POLITECNICO DI TORINO

DIPARTIMENTO DI INGEGNERIA ENERGETICA E NUCLEARE
A.a. 2024/2025
Sessione di Laurea Novembre 2025

Effect of the concentration of the support electrolyte on the performance of Anion Exchange Membrane Water Electrolysis

Candidato:
Edoardo Dionese
Relatori:
Prof. Marta Gandiglio
Co-relatori:
Prof. Massimo Santarelli
Prof. Giuseppe Sdanghi
José Carlos Martinez Rosales

Abstract

The ongoing global energy transition is driven by the urgent need to reduce greenhouse gas emissions and achieve long-term sustainability in energy production, further highlighted by geopolitical tensions. Among the various alternatives, hydrogen has emerged as a promising energy carrier due to its high gravimetric energy density and its potential to serve as a bridge between intermittent renewable sources and stable energy demand.

Water electrolysis represents the most direct and environmentally friendly pathway to produce hydrogen when powered by renewable electricity. Within this context, anion exchange membrane water electrolysis (AEMWE) has recently gained increasing attention as a hybrid technology that combines the advantages of proton exchange membrane (PEM) and alkaline systems. AEMWE enables the use of non-noble metal catalysts and less corrosive electrolytes while maintaining high ionic conductivity and compact cell design. Nevertheless, challenges remain concerning long-term stability, membrane durability, and the concentration of the supporting electrolyte, which directly affects cell efficiency and kinetics.

This thesis focuses on the influence of the support electrolyte concentration on the performance of AEMWE cells. Two electrochemical cells were assembled and tested under controlled operating conditions to isolate the effects of electrolyte concentration and feeding configuration. The experimental campaign included polarization tests, Tafel analysis, and electrochemical impedance spectroscopy (EIS). Furthermore, both dry-cathode and dual-feed modes were investigated to evaluate the role of water management and electro-osmotic transport phenomena. The analysis also involved equivalent circuit modeling through a modified Randles circuit with two constant-phase elements (CPEs), allowing for a deeper interpretation of the interfacial processes and resistive components in the system.

The results demonstrated that the electrolyte concentration has a decisive impact on both kinetic and resistive behavior of the cell. Higher electrolyte concentrations improved ionic conductivity and reduced polarization losses, leading to more stable and efficient operation. Conversely, lower concentrations increased both the activation and ohmic contributions. The comparative study between feeding modes revealed that the dry-cathode configuration ensures greater long-term stability due to more favorable water transport dynamics.

Contents

List of Figures

List of Tables

Nomenclature

AEM	Anion Exchange Membrane
AEMWE	Anion Exchange Membrane Water Electrolysis
ASR	Area-Specific Resistance
AWE	Alkaline Water Electrolyser
CCM	Catalyst Coated Membrane
CPE	Constant Phase Element
DRT	Distribution of Relaxation Time
ECM	Equivalent Circuit Modeling
EEC	Equivalent Electric Circuit
EIS	Electrochemical Impedance Spectroscopy
FAA	Formalin Aceto Alcohol
GDL	Gas Diffusion Layer
HEO	High-Entropy Oxides
HER	Hydrogen Evolution Reaction
HFR	High Frequency Resistance
IEC	Ion-Exchange Capacity
IPCC	Intergovernmental Panel on Climate Change
LDH	Lactate Dehydrogenase
LHV	Lower Heating Value
NDC	Nationally Determined Contributions
OER	Oxygen Evolution Reaction
PAES	PolyAarylene Ather Sulfone
PBP	PolyBbiphenyl Piperidinium
PEM	Proton Exchange Membrane
PFA	Perfluoroalkoxy
PGM	Platinum-Group Metals
PTFE	Polytetrafluoroethylene
SOE	Solid Oxide Electrolyser

Chapter 1

Introduction

Energy has become central to economic, social, and geopolitical debate because global demand growth—driven by industrialisation, urbanisation and population increase—has intensified pressures on finite resources and exposed system-level vulnerabilities [International Energy Agency, 2024].

Historic reliance on fossil fuels (coal, oil, and natural gas) powered long-run economic expansion but has also generated a sustained rise in greenhouse gas concentrations that drive contemporary climate change [Intergovernmental Panel on Climate Change (IPCC), 2023]. The climatic consequences of accumulated emissions are already increasing the frequency and severity of extreme events and producing tangible risks for physical infrastructure, food and water systems, and macroeconomic stability [Intergovernmental Panel on Climate Change (IPCC), 2023].

From a security perspective, energy provision and national sovereignty are tightly linked because hydrocarbon reserves remain concentrated in specific regions, a geography that has historically contributed to supply shocks and price volatility [International Energy Agency, 2024]. The 2022 disruption following Russia's invasion of Ukraine illustrated Europe's exposure to pipeline gas and spurred policy measures aimed at diversifying supplies, strengthening storage obligations and accelerating domestic clean-energy deployment [European Commission, 2022, International Energy Agency, 2024]. International climate governance has progressively established a framework for deep decarbonisation, beginning with binding targets for developed economies under the Kyoto Protocol and culminating in the universal commitments and five-yearly NDC cycle of the Paris Agreement [United Nations Framework Convention on Climate Change (UNFCCC), 2015, UNFCCC, 2021]. At the regional level, the European Green Deal and associated packages such as "Fit for 55" set out pathways to climate neutrality by mid-century through renewables expansion, electrification, efficiency improvements and grid modernisation [European Commission, 2019, European Commission / European Parliament, 2021]. Finally, the United Nations' Sustainable Development Goal 7 frames access to affordable, reliable and sustainable energy as an essential development objective for 2030 [United Nations, 2015].

Within the current policy framework, renewable energy technologies have shifted from marginal to mainstream status, supported by sustained cost reductions in solar photovoltaics and onshore wind due to learning effects, economies of scale, and supply-chain development [International Energy Agency, 2024]. Hydropower continues to provide stable low-carbon baseload, while offshore wind, geothermal, and sustainable bioenergy contribute to diversification of the generation mix [International Energy Agency, 2024]. However, the variability of solar and wind generation introduces integration challenges that require flexibility through demand response, grid reinforcement, interconnection, storage, and market mechanisms valuing capacity and ancillary services [International Energy Agency, 2024].

In this context, hydrogen has gained strategic relevance as a flexible energy carrier enabling decarbonization where direct electrification is technically or economically constrained [Intergovernmental Panel on Climate Change (IPCC), 2023, International Energy Agency, 2024]. When produced via renewable-powered electrolysis, green hydrogen can deliver near-zero direct CO_2 emissions and serve multiple roles—as a fuel, feedstock, and storage medium—linking the power, industry, and transport sectors [Intergovernmental Panel on Climate Change (IPCC), 2023, International Energy Agency, 2024]. Hydrogen thus enhances system resilience by absorbing excess renewable electricity and providing long-term storage capacity [International Energy Agency, 2024].
Despite these advantages, several barriers remain. The levelized cost of green hydrogen still exceeds fossil-based alternatives because of high electrolyzer and electricity costs, limited operating hours, and financing conditions [International Energy Agency, 2024]. Infrastructure gaps in transport, storage, and end-use adaptation—together with safety and efficiency considerations—further constrain deployment [International Energy Agency, 2024]. Consequently, policy must focus hydrogen use on hard-to-abate sectors and seasonal storage where it yields the highest system value [International Energy Agency, 2024].

Globally, governments have introduced dedicated hydrogen strategies establishing production targets, certification standards, and financial incentives such as contracts for difference, tax credits, and carbon pricing [European Commission, 2023, International Energy Agency, 2024]. In the European Union, the Hydrogen and Decarbonised Gas Market Package and REPowerEU plan define criteria for renewable fuels of non-biological origin and aim for large-scale electrolyzer deployment by 2030 [European Commission, 2023]. Building a diversified energy portfolio—centered on renewables, efficiency, digitalized demand management, and clean hydrogen—can therefore enhance energy security and reduce vulnerability to external shocks [International Energy Agency, 2024].

Chapter 2

Literature review

2.1 Electrolysis technologies

Water electrolyzers are devices that allow water to be split into hydrogen and oxygen by applying an external electrical potential across the cell, making them operate inversely compared to fuel cells. In this sense, they operate in the opposite manner to fuel cells: while fuel cells convert the chemical energy stored in hydrogen and oxygen into electricity through a spontaneous process, electrolyzers consume electricity to drive a non-spontaneous reaction. From a thermodynamic perspective, water electrolysis is characterized by a positive Gibbs free energy change, $\Delta G > 0$, which implies that the reaction requires continuous energy input to proceed. The overall electrochemical reaction can be expressed as:

$$\mathrm{H_2O(l)} \longrightarrow \mathrm{H_2(g)} + \tfrac{1}{2}\mathrm{O_2(g)}. \tag{2.1}$$

Electrolytic technology is becoming increasingly interesting for the wide range of applications in which the molecules produced by it can serve. Electrolytic technology is attracting growing interest due to the wide range of applications in which its products can serve as essential feedstocks. This trend is evident when considering the scale of research funding: investments in electrolyzer development and deployment have recently exceeded those in fuel cell projects, underlining the strategic importance of hydrogen production technologies [Hydrogeninsight, 2025]. Hydrogen production is not the only purpose of an electrolyzer [Luo, 2024]. The role of electrolyzers extends far beyond the simple production of hydrogen. These systems are capable of generating platform molecules that serve as precursors for numerous industrial processes. For instance, in addition to hydrogen, electrolyzers coupled with carbon dioxide utilization technologies can produce synthetic fuels, oils, waxes, ammonia, and synthetic polymers. In this way, electrolysis provides not only a sustainable pathway to hydrogen but also a versatile technological platform for chemical manufacturing. Furthermore, the storage of renewable energy in the form of molecular bonds represents a promising strategy for addressing the intermittency of renewable electricity sources. By converting electrical power into storable chemical energy carriers, electrolyzers offer a highly flexible solution that integrates energy production, storage, and utilization within a single framework [Bertuccioli et al., 2014].

The major categories of electrolysers can be distinguished based on their design principles and performance characteristics.

The alkaline water electrolyser (AWE) remains the most established [Research, 2025] and industrially mature [Carmo et al., 2013]. It operates using a porous separator or diaphragm, which maintains ionic conductivity between electrodes while preventing the cross-contamination of hydrogen and oxygen streams [Millet et al., 2019].
Figure 2.1 shows the AWE technology.

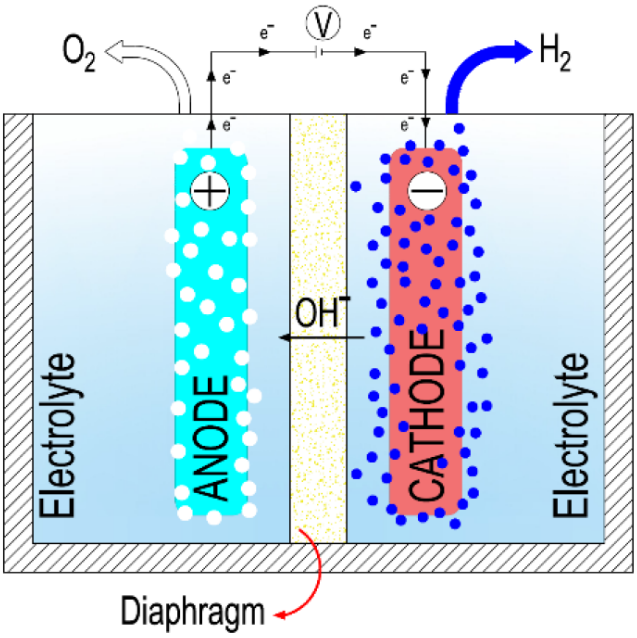

Figure 2.1: Schematic diagram of the AWE [Gavrailov and Boycheva, 2023]

A key strength of the AWE design lies in its liquid alkaline electrolyte, typically composed of potassium or sodium hydroxide, which allows the use of low-cost, non-noble metal catalysts such as nickel or iron. However, this system also exhibits some limitations — the presence of gas bubbles can hinder ionic transport within the electrolyte, and the partial mixing of gases remains a safety and efficiency concern [Bertuccioli et al., 2014]. Moreover, due to its relatively slow dynamic response, AWE technology is less suitable for direct integration with intermittent renewable energy sources [Zeng and Zhang, 2010].

Solid oxide electrolysis cells (SOECs) are emerging as one of the most promising technologies for sustainable hydrogen production. The technology is shown in Figure 2.1.

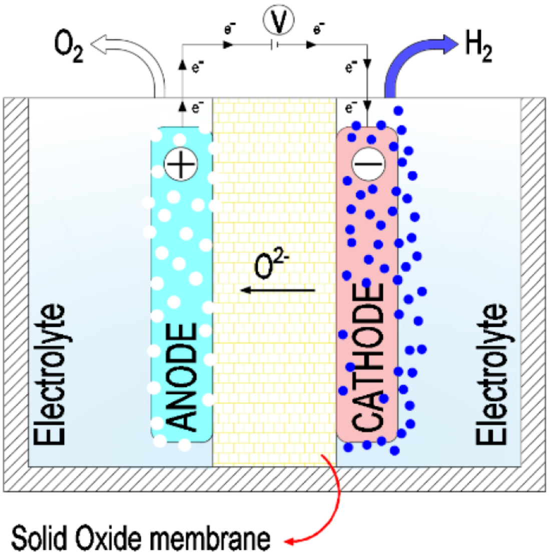

Figure 2.2: Schematic diagram of the SOEC [Gavrailov and Boycheva, 2023]

Unlike low-temperature electrolysers, SOECs operate at high temperatures, usually between 700 and 900 °C, which allows them to use both heat and electricity to split water molecules. This combination significantly improves overall energy efficiency, making the process particularly attractive when waste heat or renewable thermal sources are available [Zhou et al., 2025]. One of the main advantages of SOECs is their potentially higher efficiency compared to proton exchange membrane (PEM) or alkaline electrolysis; because reactions occur at elevated temperatures, the electrochemical losses are smaller, and the energy demand for hydrogen production decreases [Guo et al., 2025]. In addition, SOECs can perform co-electrolysis of steam and carbon dioxide, producing synthesis gas ($H_2 + CO$), a versatile feedstock for synthetic fuels — an attractive path toward “Power-to-X” applications. Nevertheless, SOEC technology faces important challenges. The high operating temperatures create severe material stresses, leading to thermal expansion mismatches and gradual degradation of electrodes and electrolytes over time: these degradation issues limit the long-term stability and durability of the system [Li et al., 2022]. Another drawback is the low operational flexibility: SOECs require pre-heating and cannot quickly adjust to variable power inputs, making them less suited for direct coupling with intermittent renewables such as solar or wind energy; finally, the cost remains a barrier, as the production of ceramic cells, sealing materials, and heat management systems is still expensive, and the technology has not yet reached large-scale commercial maturity [Zhang et al., 2024].

Solid oxide electrolysis represents an efficient and innovative route to produce hydrogen and synthetic fuels, but its industrial adoption still depends on improving durability, reducing costs, and enhancing operational flexibility.

Proton Exchange Membrane (PEM) water electrolysis is a promising technology for producing high-purity hydrogen, especially when powered by renewable energy sources [Kumar and Vurimindi, 2019]. This method operates at relatively low temperatures and offers rapid response times, making it suitable for integration with intermittent power supplies like solar and wind energy; moreover, the hydrogen produced can reach purities up to 99.999%, which is ideal for fuel cell applications and industrial processes [Kumar and Vurimindi, 2019].
Figure 2.1 explains the working methodology of PEM water electolysis.

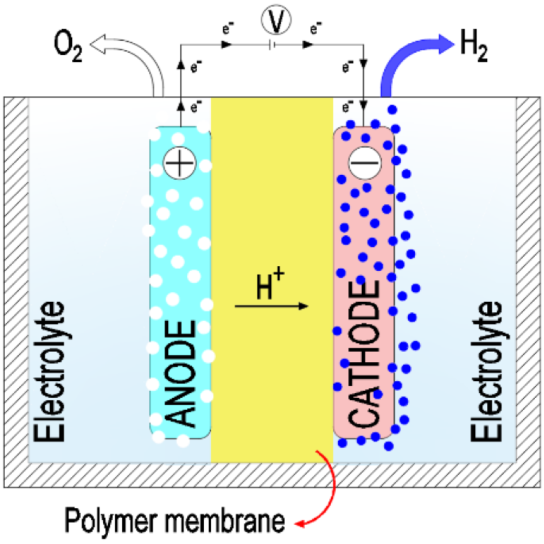

Figure 2.3: Schematic diagram of the PEMWE [Gavrailov and Boycheva, 2023]

However, PEM electrolysis faces challenges related to the cost and durability of its components [Sezer, 2025]. The use of precious metals such as platinum and iridium in electrocatalysts contributes to high material costs, which remain a significant barrier to large-scale adoption; additionally, the long-term stability of these materials under operational conditions is a concern, as degradation can lead to reduced efficiency and increased maintenance needs [Sezer, 2025].
Recent research has focused on developing cost-effective and durable alternatives to traditional electrocatalysts [Wang et al., 2025]. For instance, studies have explored the use of non-precious metal-based catalysts and novel membrane materials to enhance performance and reduce costs [Wang et al., 2025]. Moreover, advancements in system design and operational strategies aim to improve the overall efficiency and lifespan of PEM elec-

trolyzers [Wang et al., 2025].
While PEM water electrolysis holds significant potential for sustainable hydrogen production, addressing the challenges of cost and durability is crucial for its widespread implementation [Sezer, 2025].

Anion exchange membrane water electrolysis has emerged as a promising technology for sustainable hydrogen production, combining the advantages of both alkaline and proton exchange membrane (PEM) systems [Chand et al., 2022, George and Singh, 2025]. Its ability to employ non-noble metal catalysts significantly lowers material costs while maintaining high efficiency under mildly alkaline conditions [Seitz and Marshall, 2022, Nguyen et al., 2023]. This hybrid configuration enables AEMWE to operate with lower-cost components, potentially bridging the gap between traditional AWE and PEM technologies [Smith et al., 2022a]. The technology is shown in Figure 2.4.

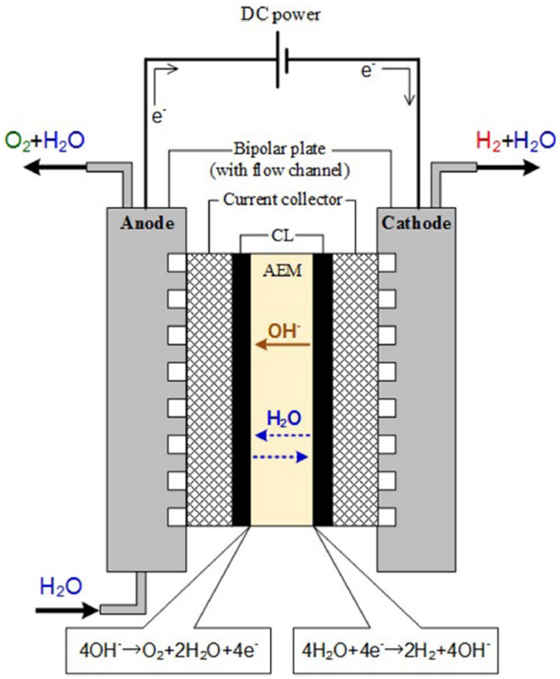

Figure 2.4: Schematic of the AEMWE [Ito et al., 2018]

Despite substantial progress, several obstacles remain. The durability of anion-exchange membranes and the stability of catalysts under high hydroxide flux are still limiting factors [Chen et al., 2022a, Wang et al., 2023]. Catalyst reconstruction and gradual membrane degradation can reduce long-term performance, particularly when operating with pure water feeds [Lopez et al., 2025]. Even though recent prototypes have achieved energy efficiencies around 75% for over 2000 operational hours, further advancements in electrode architecture and water management are necessary [Smith et al., 2022a, Zhao et al., 2024]. Ongoing work explores improved polymer structures, more robust interfaces, and scalable stack designs to achieve gigawatt-scale hydrogen systems [Wang et al., 2023]. AEMWE stands as a flexible and cost-effective alternative for sustainable hydrogen production. Its success will depend on solving challenges in membrane stability, catalyst durability, and standardized testing to ensure reproducible and efficient long-term operation [Lopez et al., 2025, Nguyen et al., 2023, Wang et al., 2023].

2.2 Fundamental principles of AEM Water Electrolysis

In an AEMWE cell, hydroxide ions (OH^-) migrate from the cathode side through a polymeric anion exchange membrane to the anode side, completing the ionic circuit [Chand et al., 2022]. The overall water electrolysis reaction under alkaline conditions can be written as:

$$\mathrm{H_2O(l)} \rightarrow \tfrac{1}{2}\mathrm{O_2(g)} + \mathrm{H_2(g)} \tag{2.2}$$

At the cathode, the hydrogen evolution reaction (HER) occurs:

$$\mathrm{2H_2O + 2e^- \rightarrow H_2 + 2OH^-} \tag{2.3}$$

At the anode, the oxygen evolution reaction (OER) proceeds:

$$\mathrm{4OH^- \rightarrow O_2 + 2H_2O + 4e^-} \tag{2.4}$$

Together, these are the three principal reactions that govern water splitting in an AEMWE: the full cell reaction, HER, and OER.

In practical devices, the cell voltage required to drive these reactions is higher than the thermodynamic minimum ($\sim$1.23 V) due to overpotentials, resistive losses, and membrane ohmic drop [Ito et al., 2018]. The total cell voltage V_{cell} can be decomposed into the sum of the reversible potential E_{rev} and all overvoltage contributions:

$$V_{\mathrm{cell}} = E_{\mathrm{rev}} + \eta_{\mathrm{act,an}} + \eta_{\mathrm{act,cat}} + \eta_{\mathrm{ohm}} + \eta_{\mathrm{conc}} \tag{2.5}$$

Here, $\eta_{\mathrm{act,an}}$ and $\eta_{\mathrm{act,cat}}$ are the activation overpotentials at the anode and cathode, respectively, η_{ohm} represents ohmic losses through membranes and interfaces, and η_{conc} includes concentration or transport limitations ([Chand et al., 2022]). Activation overvoltages $\eta_{\mathrm{act,an}}$ are strongly dependent on catalyst design and surface phenomena. For

OER catalysts such as NiFe or layered mixed-metal oxides, $\eta_{\text{act,an}}$ values in the range of 280–350 mV at 10 mA cm^{-2} are common in alkaline environments [Smith et al., 2024, Qi et al., 2025]. On the cathode side, advanced HER catalysts like Ni–Mo alloys or Ni/CeO_x interfaces often exhibit activation overpotentials of 80–120 mV under similar current densities [Smith and Lee, 2025, Tanaka and Kimura, 2025].

Ohmic losses η_{ohm} are dominated by ionic resistance within membranes, contact resistances in electrodes, and the conductivity of ionomers or electrolyte pathways. Commercial anion exchange membranes typically demonstrate conductivity in the order of 30 to 60 mS cm^{-1} at 60–80 °C, resulting in ohmic drops on the order of 100–250 mV at 1 A cm^{-2} [Chen et al., 2022a].

Concentration overvoltages η_{conc} become significant primarily at high current densities (above $\approx$ 3 A cm^{-2}), where gas bubble formation, depletion of reactants near the electrode surface, or inadequate mass transport impose additional voltage penalties [Zhang et al., 2023].

A commonly used empirical relation linking overvoltage to current density is the Tafel equation:

$$\eta = a + b\log_{10}(i) \tag{2.6}$$

where a is a constant related to the exchange current density and b is the Tafel slope. For well-engineered OER catalysts in alkaline media, b often lies between 30 and 40 mV dec^{-1}, while for HER catalysts it can be in the 80–120 mV dec^{-1} range [Wang et al., 2024, Rosman et al., 2025]. This logarithmic scaling means that even small increases in current density demand notable increases in applied overvoltage, which is one of the reasons designing high-performance catalysts is so critical [Montalto et al., 2025].

Typical operating voltages for modern AEMWE systems lie in the range of 1.6 to 1.8 V at current densities of 0.5–1.0 A/cm^2 [Qi et al., 2025, Rosman et al., 2025]. In favorable designs, efficiencies (based on lower heating value, LHV) of 60–70% are reported under steady operation [Montalto et al., 2025].

The performance of an AEMWE cell depends critically on the kinetics of HER and OER, the ionic conductivity of the membrane, and the interfacial resistances. For HER, catalysts must facilitate the adsorption of protons and evolution of molecular hydrogen, often at low overpotential. For OER, catalysts must efficiently facilitate the multi-step oxidation of hydroxide ions to oxygen gas without excessive energy loss [Rosman et al., 2025]. Because OER is much slower and more energy-intensive, most design efforts focus on improving OER catalysts while ensuring HER remains efficient [Chand et al., 2022].

Another major consideration is the transport of hydroxide ions through the membrane.

Ionic resistance and water management (i.e., supply and removal of water) contribute significantly to the total voltage loss. In addition, the membrane must maintain chemical stability in alkaline environments and moderate mechanical strength. Degradation mechanisms such as carbonate formation can reduce membrane conductivity over time [Chen et al., 2022a].

2.2.1 Catalysts in AEMWE

A key component that determines the overall performance, efficiency, and lifetime of AEMWE devices is the electrocatalyst [Ito et al., 2018, Rosman et al., 2025]. Catalysts drive both the HER and the OER, processes that require high activity, stability, and resistance to degradation [Chand et al., 2022, Montalto et al., 2025, Qi et al., 2025]. Over the past few years, researchers have focused on developing transition-metal-based catalysts as cost-effective and durable alternatives to precious metals traditionally used in electrolysis systems [Wang et al., 2024, Smith et al., 2024].

Nickel and iron remain the most important materials for AEMWE catalysis, particularly for OER applications (Wang et al. [2024], Rosman et al. [2025]). Their relatively low cost, abundance, and electronic structure make them effective for promoting oxygen evolution in alkaline environments [Montalto et al., 2025]. Recent investigations have demonstrated that modifying NiFe catalysts with additional elements can significantly improve their activity (Qi et al. [2025]). For example, the incorporation of titanium into nickel ferrite ($NiFe_2O_4$) structures enhances electrical conductivity and optimizes oxygen binding energy, leading to better kinetic performance during electrolysis [Smith et al., 2024]. Similarly, amorphous NiFe catalysts stabilized through borate bridging exhibit improved durability and reduced structural degradation under industrial current densities [Qi et al., 2025]. These studies highlight the importance of microstructural tuning and chemical stabilization to prolong catalyst lifespan [Montalto et al., 2025].

Expanding beyond conventional NiFe materials, high-entropy oxides (HEOs) and spinel-type structures have recently attracted attention for their ability to maintain structural integrity under prolonged operation [Montalto et al., 2025]. Composed of multiple transition metals such as Ni, Co, Fe, Mn, and Mg, these HEO catalysts leverage configurational entropy to resist phase segregation, while spinel configurations enhance charge transfer and surface area, resulting in improved current densities in AEMWE cells [Rosman et al., 2025]. Performance metrics for AEMWE catalysts are typically evaluated in terms of current density, overpotential, Tafel slope, and stability under operational conditions [Chand et al., 2022]. As shown in Table 2.1, the combination of HEO design and NiFe engineering offers a pathway toward high-performance, scalable anodes capable of sustaining multi-ampere current densities at operational voltages between 1.6 and 2.2 V, extending to over 4 A/cm^2 at 2.2 V, while maintaining excellent structural integrity during prolonged operation [Montalto et al., 2025, Rosman et al., 2025].

Table 2.1: Performance summary of Spinel HEO (Ni–Co–Mn) catalyst

Main Reaction	OER
Current Density (A cm^{-2}) @ V$_{\text{cell}}$ (V)	1.6 @ 1.8 V ; 4.1 @ 2.2 V
Overpotential (mV, 10 mA cm^{-2})	$\approx$ 300
Durability / Conditions	>100 h stable
Source	Montalto et al. [2025], Rosman et al. [2025]

Transition-metal-based catalysts, including oxides, sulfides, and phosphides, have also gained attention for their promising bifunctional activity toward both HER and OER [Rosman et al., 2025]. These materials can operate efficiently without relying on precious metals, offering a more scalable path toward commercial AEMWE applications [Ito et al., 2018, Wang et al., 2024]. Table 2.2 shows a platinum-group-metal-free (PGM-free) AEMWE operated at 80 °C, Nickel-molybdenum Ni_4Mo cathode coupled with a NiFe anode; this configuration improves HER kinetics by tuning the hydrogen adsorption energy on Ni sites, and it achieved 1 A cm^2 at 1.75 V, enabling efficient hydrogen production at current densities exceeding 3 A/cm^2 [Smith and Lee, 2025].

Table 2.2: Performance summary of Ni_4Mo alloy catalyst

Main Reaction	HER
Current Density (A cm^{-2}) @ V$_{\text{cell}}$ (V)	1 @ 1.75 V ; 3 @ >1.9 V
Overpotential (mV, 10 mA cm^{-2})	<100
Durability / Conditions	Stable up to 80 °C
Source	Smith and Lee [2025]

Catalyst reconstruction during operation is a key factor influencing long-term stability [Chen et al., 2022a]. Studies have revealed that NiFeCo-based electrodes undergo surface rearrangements and metal dissolution under continuous potential cycling, affecting both the catalytic efficiency and the mechanical integrity of the electrodes [Chen et al., 2022b]. The use of amorphous catalysts and flexible supports has proven effective in minimizing such degradation; furthermore, integrating dopants such as boron or molybdenum can improve corrosion resistance while preserving catalytic activity [Qi et al., 2025, George and Singh, 2025]. Despite these advances, maintaining stable performance over thousands of hours remains a significant challenge for commercial AEMWE systems [Chen et al., 2022a].

According to the analysis reported by Ahmed and Fowler (2024), a carefully optimized Ni–Fe–Co composition supports current densities above 1.5 A $^{-2}$ at 2.1 V, and approaches 1.9 A $^{-2}$ at 2.2 V under standard AEMWE operating temperatures of 55–70 °C. Their work in 2.3 also shows that adjusting the Fe content to roughly 5 wt% substantially decreases the oxygen evolution overpotential, achieving values close to 228 mV at 10 mA $^{-2}$, while preserving stable behaviour over extended electrolysis periods [Ahmed and Fowler, 2024].

Table 2.3: Performance summary of NiFeCoO$_x$ catalysts for AEM water electrolysis.

Main Reaction	OER
Current Density (A cm^{-2}) @ V$_{\text{cell}}$ (V)	1.52 A cm^{-2} @ 2.1 V (55°C); 1.62 A cm^{-2} @ 2.1 V (70°C).
Overpotential (mV, 10 mA cm^{-2})	$\sim$228 mV
Durability / Conditions	Stable high-current operation.
Source	Ahmed and Fowler [2024]

At the same time, the development of unified NiFeOOH anodes, shown in Table 2.4, has shown how phase engineering can maximize OER turnover while ensuring robustness at industrial current densities [Park et al., 2025]. Park et al. (2025) achieved current densities of 4.9 A cm^{-2} at 1.9 V and 8.0 A $^{-2}$ at 2.05 V, sustaining 1000 mA cm^{-2} for more than 350 hours with negligible degradation. These results position NiFeOOH as a viable architecture for scalable alkaline electrolysis stacks, offering a route to high-current, durable operation without precious metals.

Table 2.4: Performance summary of NiFeOOH unified catalyst

Main Reaction	OER
Current Density (A cm^{-2}) @ V$_{\text{cell}}$ (V)	4.9 @ 1.9 V ; 8.0 @ 2.05 V
Overpotential (mV, 10 mA cm^{-2})	—
Durability / Conditions	350 h @ 1 A cm^{-2}
Source	Park et al. [2025]

Ongoing research is directed toward multi-metallic catalysts, nanostructured electrodes, and hybrid organic-inorganic membranes that can enhance both catalytic efficiency and

ion conductivity [Rosman et al., 2025, Montalto et al., 2025].
Nevertheless, catalyst poisoning remains a major challenge: impurities such as carbonate ions, metal cation migration, and membrane degradation products can adsorb onto active sites, hindering electron transfer and reducing activity [Smith et al., 2024]. The surface oxidation of nickel and iron-based catalysts, while beneficial to a certain extent, can also lead to deactivation when oxide layers become too thick or electronically insulating [Chand et al., 2022]. Strategies to mitigate poisoning include surface engineering, protective coatings, and electrolyte optimization [Ito et al., 2018, Chen et al., 2022a].

2.2.2 Membrane materials in AEMWE

The membrane in an AEMWE cell must combine high hydroxide ion conductivity, excellent mechanical stability, low gas permeability, and long-term alkaline durability [Zheng et al., 2024]. Designing materials that satisfy these multiple constraints simultaneously remains a core scientific challenge.

The intrinsic mobility of hydroxide ions is lower than that of protons, which leads to higher ohmic resistance and slower charge transport in AEM systems [Mamlouk and Scott, 2015]. Therefore, polymers with high ion-exchange capacity (IEC) and continuous ionic pathways are necessary to maintain competitive performance. However, increasing the IEC often causes excessive water uptake and swelling, which can compromise dimensional stability [Hu et al., 2021]. Balancing conductivity and mechanical integrity has thus become a key target in polymer design for AEMWEs.

Among the most successful polymeric systems are those based on rigid aromatic backbones and stable cyclic cationic groups such as piperidinium. The commercial PiperION membranes exemplify this approach, using an ether-free poly(aryl piperidinium) backbone functionalized with piperidinium cations [Endrődi et al., 2020]. This structure enhances alkaline durability and allows fabrication of thin, mechanically robust films. As shown in Table 2.5, Endrődi et al. demonstrated that PiperION membranes could maintain high carbonate ion conductance and low voltage losses under CO_2 electrolysis conditions, even after extended exposure to 1 M KOH at 100°C for 2000 hours [Endrődi et al., 2020].

Recent developments have shown that microstructuring of PiperION surfaces further improves the interfacial contact between the membrane and electrodes. Mechanical compression followed by dehydration can “lock in” micro-patterns that enhance ionic transport and reduce interfacial resistance, leading to improved cell performance and durability [Yassin et al., 2025]. Moreover, the inclusion of controlled ionomer loading in the cata-

Table 2.5: Performance summary for the PiperION membrane

Parameter	**Description**
Membrane type	PiperION (ether-free poly(aryl piperidinium))
Functional group	Cyclic piperidinium cations
Electrode materials	Ag nanoparticles on carbon paper (cathode); IrO_x coated Ti (cathode)
Supporting electrolyte	1 M KOH
Performance	Stable for 2000 h at 100 °C; high carbonate ion conductance; ≈ 15 µm reinforced film
Reference	Endrődi et al. [2020]

lyst layers has been found to minimize overpotential while maintaining high active area utilization [Volk et al., 2025].

Table 2.6: Performance summary for the PAES–mPip membrane

Parameter	**Description**
Membrane type	Poly(arylene ether sulfone) with multiple piperidinium side chains
Functional group	Flexible quaternary ammonium (piperidinium)
Electrode materials	$NiFe_2O_4$/Ni (anode); Ni foam (cathode)
Supporting electrolyte	2 M NaOH
Performance	$\sigma_{OH^-} > 100$ mS cm^{-1} @ 80 °C; 88% retention after 480 h in 2 M NaOH
Reference	Hu et al. [2021]

From a molecular design perspective, Hu et al. introduced multiple flexible side-chain piperidinium groups into a poly(arylene ether sulfone) backbone (Table 2.6), achieving conductivities above 100 mS/cm at 80°C and over 88% retention after 480 h in 2 M NaOH at 80°C [Hu et al., 2021].

In contrast, Nafion —the archetypal proton exchange membrane— has limited applicability in alkaline environments. Nafion's perfluorinated backbone with sulfonic acid terminal groups provides excellent proton conduction in acidic media but degrades rapidly under alkaline conditions [Smith et al., 2022b]. As shown in Table 2.7, attempts to convert Nafion precursors into anion-conducting forms through quaternization of sulfonyl fluoride intermediates have yielded materials with moderate hydroxide conductivity but poor long-term stability in strong base [Smith et al., 2022b, Salerno et al., 2013]. As a result,

Table 2.7: Performance summary for the Nafion-derived AEM

Parameter	Description
Membrane type	Quaternary ammonium-bearing perfluorinated polymer derived from Nafion or Aquivion
Functional group	Trimethylammonium quaternary groups
Electrode materials	$NiFe_2O_4$/Ni mesh (anode); Ni foam (cathode)
Supporting electrolyte	1 M KOH
Performance	$\sigma_{OH^-} \approx 40$ mS cm^{-1} @ 80 °C; degraded within days in strong base
Reference	Smith et al. [2022b], Salerno et al. [2013]

Nafion-derived AEMs serve mainly as benchmarks rather than practical membranes for AEMWE applications.

Table 2.8: Performance summary for the Polyxanthene–PBP membrane

Parameter	Description
Membrane type	Crosslinked polyxanthene–poly(biphenyl piperidinium)
Functional group	Piperidinium-based quaternary ammonium
Electrode materials	NiFe LDH / Ni mesh (anode); Ni foam (cathode)
Supporting electrolyte	2 M KOH
Performance	$\sigma_{OH^-} = 96$ mS cm^{-1} @ 80 °C; stable 1000 h in 2 M KOH
Reference	Zheng et al. [2024]

Beyond PiperION and Nafion derivatives, other promising cases include crosslinked polyxanthene–poly(biphenyl piperidinium) AEMs with ultramicroporous morphology, which combine high hydroxide conductivity (96 mS/cm at 80°C) with excellent mechanical strength and alkaline stability [Zheng et al., 2024]. Performances are shown in Table 2.8.

Complementary approaches focus on mechanical reinforcement and thin composite membranes. Sangmyung University researchers developed pore-filling AEMs that showed superior tensile strength and durability compared to commercial FAA-3 and PiperION membranes, emphasizing the interplay between thickness, mechanical stress, and ion transport [Choi et al., 2024].

Table 2.9: Performance summary for the PFAEM membrane.

Parameter	**Description**
Membrane type	Acrylamide-based pore-filling anion exchange membrane (PFAEM)
Functional group	Amide-based quaternary ammonium
Electrode materials	Ni foam / NiMo
Supporting electrolyte	1 M KOH
Performance	Superior durability vs FAA-3; enhanced gas separation
Reference	Choi et al. [2024]

2.2.3 Electrochemical Impedance Spectroscopy

EIS is recognized as one of the most insightful and non-destructive diagnostic tools for understanding the electrochemical behavior of systems such as AEMWEs [Hallemans et al., 2023]. By applying a small sinusoidal voltage or current perturbation and analyzing the frequency-dependent response, EIS allows the separation of individual physical processes that contribute to the total impedance of a device [Hallemans et al., 2023]. In AEMWE systems, this capability is crucial because multiple loss mechanisms—ohmic, charge-transfer, and mass transport—often overlap across frequency domains, making it difficult to distinguish their respective effects using steady-state techniques [Pushkarev et al., 2023].

In these electrolyzers, the anion exchange membrane (AEM) plays a central role in ensuring ionic transport, gas separation, and mechanical stability [Bernat et al., 2024]. It selectively conducts hydroxide ions between the electrodes while preventing the mixing of hydrogen and oxygen products [Watzele et al., 2024]. Its structural integrity, hydration level, and chemical stability under strongly alkaline conditions determine its resistance and thus its contribution to the overall cell impedance [Bernat et al., 2024]. Because the membrane is one of the primary ohmic components, its resistance typically appears at the high-frequency intercept of the Nyquist plot [Watzele et al., 2024]. In practical EIS spectra, one generally observes a real-axis intercept corresponding to ohmic resistance, followed by one or more semicircular arcs that represent polarization or charge-transfer processes [Vincent et al., 2021]. At lower frequencies, a linear tail or secondary arc can emerge due to mass transport or concentration polarization effects, particularly when diffusion or bubble accumulation becomes limiting [Ranz et al., 2024].

To better deconvolute overlapping contributions, two complementary analytical approaches have gained popularity: equivalent circuit modeling (ECM) —or equivalent electric circuit (EEC)— and distribution of relaxation times (DRT) [Ranz et al., 2024]. ECM approximates the cell with a network of electrical elements—resistors, capacitors, constant-phase elements, and sometimes Warburg diffusion components—to represent electrochemical phenomena [Vincent et al., 2021]. DRT reconstructs the impedance spectrum as a continuous distribution of characteristic time constants, allowing the identification of discrete peaks corresponding to distinct physical mechanisms [Ranz et al., 2024]. For example, Ranz et al. (2024) applied combined full-cell and half-cell EIS together with DRT to separate contributions from the HER, OER, ionic transport in catalyst layers, and interfacial resistances, identifying up to five distinct relaxation features [Ranz et al., 2024].

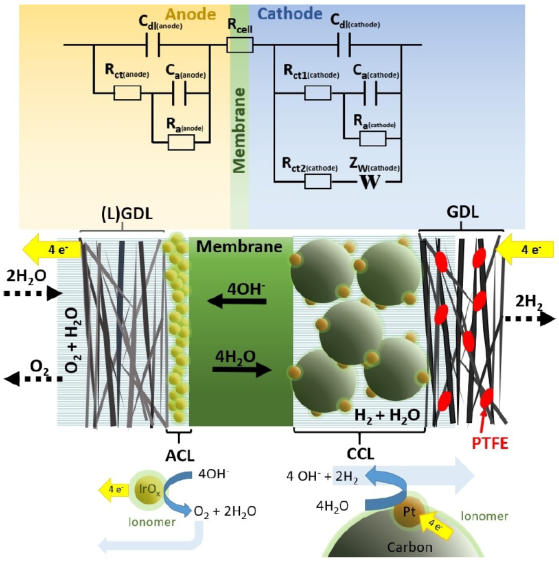

Figure 2.5: Equivalent electric circuit (EEC) and AEM MEA scheme.
[Watzele et al., 2024]

In constructing an equivalent circuit for AEMWE, the ohmic resistance R_{ohm} is generally placed in series with two parallel branches representing the anodic and cathodic interfaces, each modeled as R_{ct} in parallel with a CPE, as shown in Figure 2.5 [Vincent et al., 2021, Watzele et al., 2024]. This configuration reflects the kinetic and capacitive characteristics of each electrode, while an optional Warburg element Z_W may be added to account for diffusion limitations [Watzele et al., 2024]. The CPE component models non-ideal capacitive behavior due to surface roughness, porosity, and distributions of relaxation times within heterogeneous catalyst layers [Watzele et al., 2024].

Modified Randles Equivalent Circuit with CPE

Among the many models used to interpret EIS data, the modified Randles equivalent circuit with a CPE remains one of the most versatile and physically meaningful [Randles, 1947, Macdonald, 1992, Orazem and Tribollet, 2017, Lazanas et al., 2023]. This

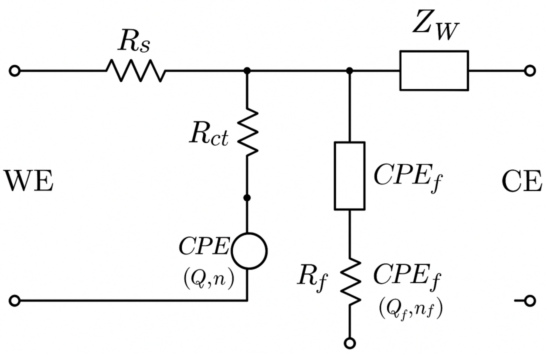

Figure 2.6: Modified Randles equivalent electric circuit. Concept adapted from Orazem and Tribollet [2017], Lazanas et al. [2023].

model extends the classical Randles circuit—originally proposed for simple redox reactions—by substituting the ideal double-layer capacitor with a CPE that accounts for non-ideal interfacial behavior [Randles, 1947, Orazem and Tribollet, 2017]. The basic structure comprises the solution resistance R_s in series with a parallel branch combining the charge-transfer resistance R_{ct} and a CPE, while optional diffusion components such as the Warburg element Z_W can be included [Macdonald, 1992, Orazem and Tribollet, 2017].

The CPE is defined by its admittance:

$$Y(\omega) = Q(j\omega)^n \tag{2.7}$$

where Q (in $\mathrm{F\,s}^{n-1}$) represents the pseudo-capacitance and n ($0 < n \leq 1$) quantifies deviation from ideal capacitive behavior. When $n = 1$, the CPE becomes an ideal capacitor; when $n < 1$, it represents a distributed or fractal-like capacitance due to surface heterogeneity [Brug et al., 1984, Orazem and Tribollet, 2017].

The total impedance of the simplified Randles-CPE circuit (without Warburg term) can be written as:

$$Z(\omega) = R_s + \frac{R_{ct}}{1 + (j\omega R_{ct} Q)^n} \tag{2.8}$$

and, when a Warburg diffusion term $Z_W = \sigma/\sqrt{j\omega}$ is included, the full model becomes:

$$Z(\omega) = R_s + \left[\frac{1}{R_{ct}^{-1} + (Q(j\omega)^n) + Z_W^{-1}} \right]^{-1} \tag{2.9}$$

where σ is the Warburg coefficient.

Parameter extraction in EIS is typically performed through *nonlinear least-squares fit-*

ting, where the measured complex impedance data are matched to a selected equivalent circuit model. This process yields the numerical values of circuit elements such as the solution resistance R_s, the charge-transfer resistance R_{ct}, the CPE parameters Q and n, and, when relevant, additional terms such as the film resistance R_f, the film CPE Q_f, n_f, and the diffusion parameters associated with the Warburg element [Orazem and Tribollet, 2017, Lazanas et al., 2023].

However, since the constant-phase element CPE does not behave as an ideal capacitor unless $n = 1$, its parameter Q cannot be interpreted directly as a true capacitance[Brug et al., 1984, Orazem and Tribollet, 2017].

To make meaningful comparisons between systems, empirical relationships have been developed to convert Q into an *effective double-layer capacitance* (C_{eff}). The most widely used conversion is the *Brug relation*, later refined by Hsu and Mansfeld, which expresses C_{eff} as:

$$C_{\text{eff}} = \left(QR_{ct}^{1-n}\right)^{1/n} \tag{2.10}$$

This expression accounts for both the CPE's frequency dispersion (n) and the resistance scale of the system (R_{ct}), effectively normalizing the non-ideal capacitance to a physically interpretable quantity [Brug et al., 1984, Hsu and Mansfeld, 2001, Chang, 2020].

In practical terms, C_{eff} represents the real, frequency-independent equivalent capacitance that an ideal capacitor would have if it produced the same charge-storage behavior as the observed non-ideal interface. A high C_{eff} value typically indicates a large electrochemically active area or enhanced ion accumulation capacity at the interface, whereas a low C_{eff} may signal passivation, dehydration, or reduced active surface availability [Orazem and Tribollet, 2017, Lazanas et al., 2023].

Chapter 3

Methodology

3.1 Experimental setup

The experimental setup consists of a closed-loop circuit, shown in Figure 3.1. At the center of the loop is the main electrolytic cell, which employs a PiperION membrane with an active area of 25 cm^2 as the primary electrolyte.

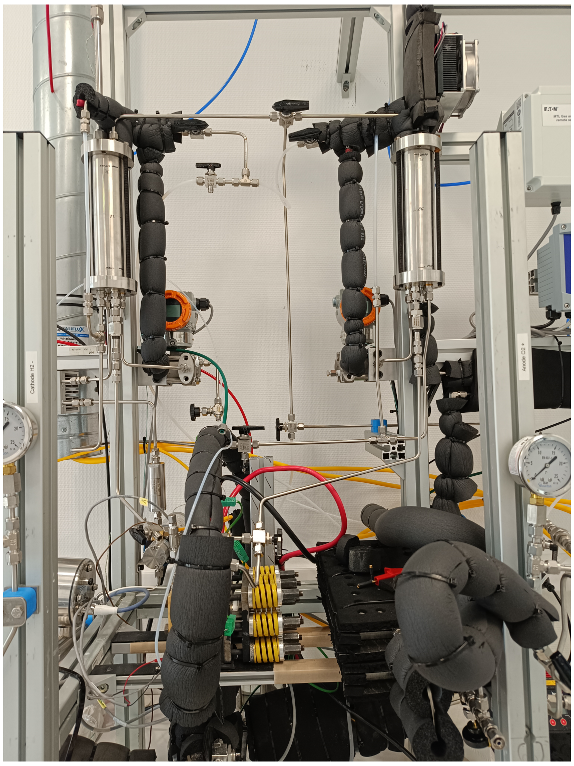

Figure 3.1: Experimental setup

The supporting electrolyte used throughout the system is a potassium hydroxide (KOH) solution, used in two different concentrations (0.1 M and 1 M), which provides ionic conductivity and enables efficient operation of the electrochemical cell.

At the bottom section of the loop, two insulated heat exchangers are connected to the electrolyzer to ensure proper thermal regulation during operation; one of them coated with a thermal insulating material is shown in Figure 3.2d. Temperature control is essential to maintain constant electrochemical performance and to prevent degradation of both the membrane and the electrolyte. On the front face of the electrolyzer, hydrogen outlet tubing is connected, while on the rear face the water inlet and the electrical power supply connections are located, as shown in Figure 3.3b.
The supporting electrolyte (KOH) enters and exits the electrolyzer through tubing positioned on the upper and lower faces of the cell.

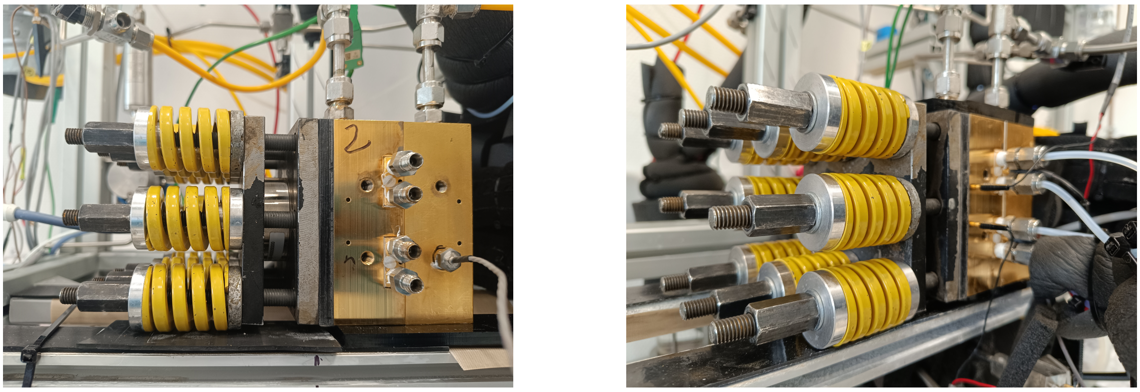

(a) Electrolyser cell, frontal view

(b) Electrolyser cell, 9 springs detail

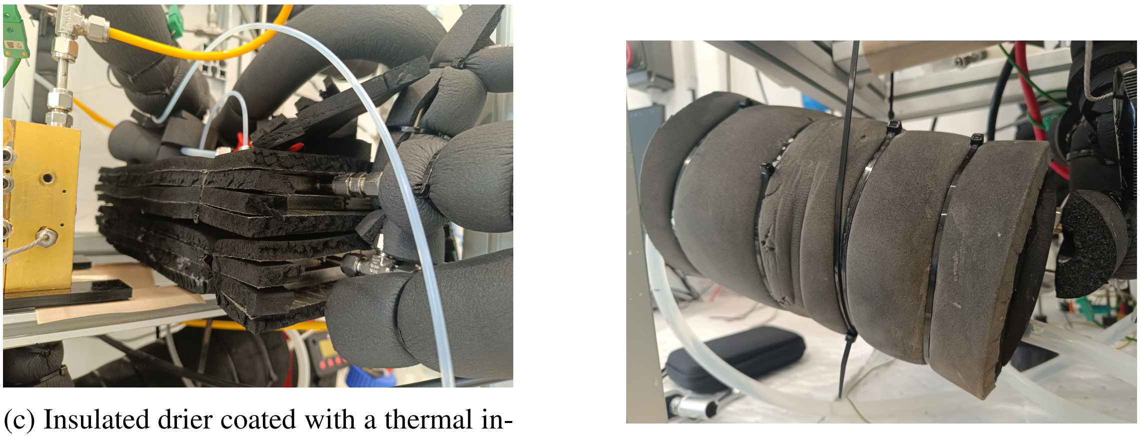

(c) Insulated drier coated with a thermal insulating material

(d) Insulated heat exchanger

Figure 3.2: Experimental setup details

On the right-hand side of the loop, an insulated dryer unit is installed to maintain the electrolyte concentration constant throughout the experiment. This component, shown in

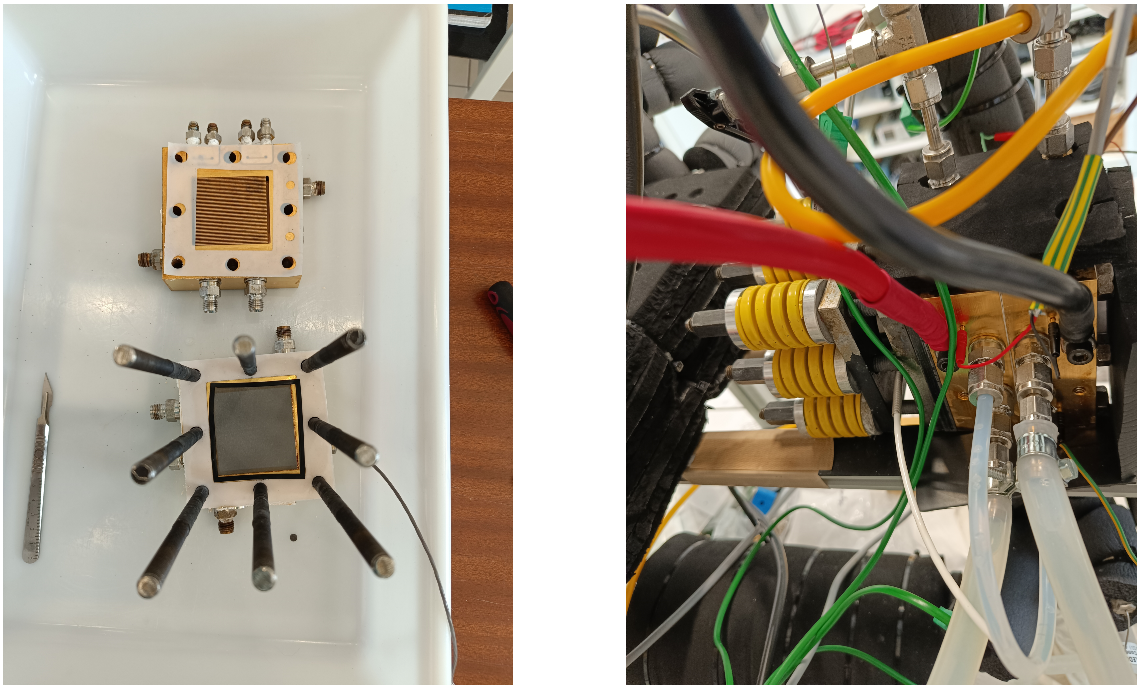

(a) Cell assembly

(b) Rear of the cell

Figure 3.3: Cell details

Figure 3.2d, removes excess moisture and helps prevent variations in KOH molarity that could affect the conductivity and performance of the electrolyzer. The dryer is equipped with a valve system that allows it to be bypassed when drying is not required, providing flexibility during operation and minimizing unnecessary pressure losses in the circuit.

Both the anode and cathode lines are equipped with dedicated monitoring units that provide real-time measurements of the electrolyte properties. Each line is fitted with a display connected to two thermocouples installed on the upper side and to a probe system capable of measuring both the conductivity and the temperature of the circulating fluid.
The conductivity is expressed in Siemens per centimeter (S cm^{-1}) and serves as a key indicator of the electrolyte's ionic strength and stability during operation. Monitoring both conductivity and temperature at both electrodes allows the detection of possible concentration gradients or dilution effects that may occur because of electro-osmotic drag or water transport through the membrane.

Two flow meters are positioned along the horizontal section to measure the electrolyte flow rate on both sides of the loop. The data from these instruments are used to evaluate the hydraulic stability of the system and to verify that uniform flow conditions are maintained during testing.

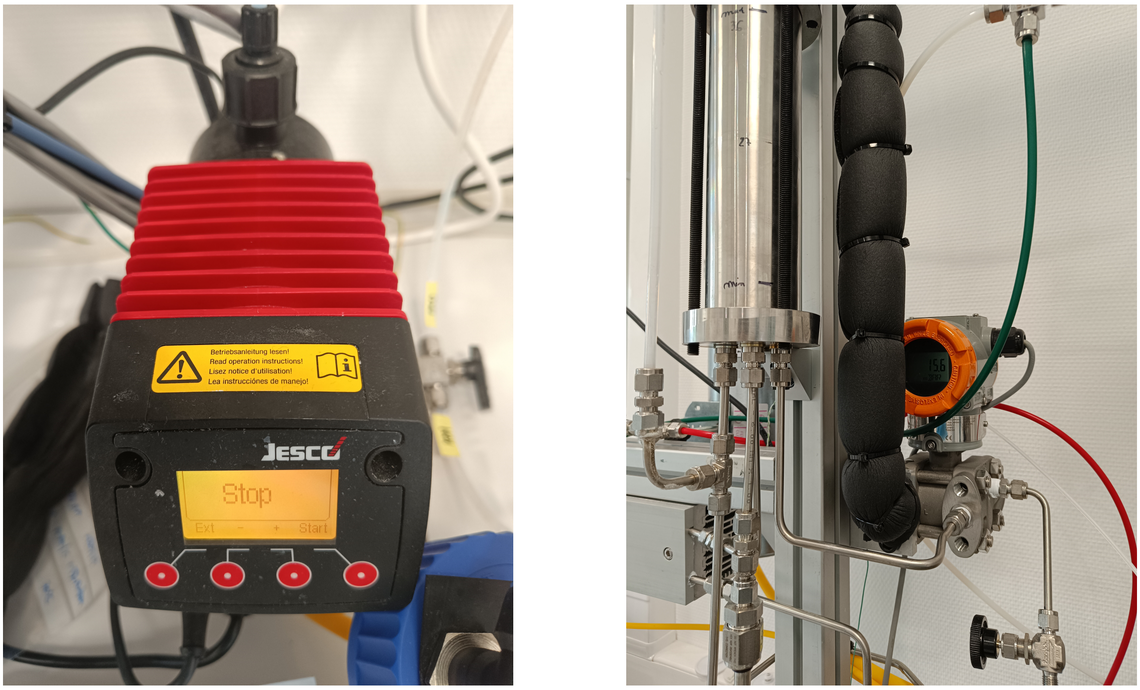

(a) Pump

(b) Liquid-level detector

Figure 3.4: Loop detail

On each side of the loop, there is a dedicated reservoir for the supporting electrolyte. Each reservoir is connected to a liquid-level detector Figure 3.4b that measures the internal pressure in millibars (mbar). This signal is assumed to represent a relative pressure value, which increases as liquid is pumped into the reservoir and decreases when the liquid level drops. This measurement provides indirect feedback on the electrolyte volume circulating within the system.

To promote electrolyte circulation and purging, the circuit is connected to a nitrogen supply line. Nitrogen is used due to its inert nature, ensuring that no undesired chemical reactions occur with either the electrolyte or the system components. The KOH solution is initially contained in a 1 L storage tank, from which it is circulated through the loop using a pump (Figure 3.4a). The pump ensures continuous flow through the electrolyzer and auxiliary components, thereby stabilizing both the electrolyte composition and temperature during operation.

At the beginning of each experiment, the entire loop is filled with the supporting electrolyte (KOH solution). This initial circulation phase allows the system to reach steady-state thermal and hydraulic conditions and ensures that all internal surfaces of the electrolyzer and auxiliary components are properly wetted. The KOH is circulated either through both the anode and cathode compartments or, in some cases, only through the anode side, depending on the specific configuration under investigation.

Once the system is fully conditioned and stable, the experimental phase is initiated. At this stage, the inlet liquid is switched from the KOH solution to pure deionized water. The deionized water is stored in a 5 L glass vessel and circulated through the same pumping system previously used for the KOH. The use of deionized water is essential to prevent the introduction of ionic contaminants that could interfere with the electrochemical reactions, alter the conductivity of the electrolyte, or induce undesired deposition phenomena on the membrane or electrodes. Its high purity ensures reproducible electrochemical behavior and minimizes degradation of the PiperION membrane and other system components.
To ensure stable operation and protect the components of the electrolytic loop, both the anode and cathode lines are equipped with dedicated filtration and pressure monitoring systems. Each line includes an in-line filter positioned upstream of the electrolyzer. These filters are designed to remove any particulate contaminants or residues that may form during operation, thereby preventing clogging, minimizing membrane fouling, and ensuring clean electrolyte circulation through the system.

Temperature control during operation is achieved using a Julabo thermostatic bath. The Julabo circulates water maintained at a constant temperature of 60 °C, which is transferred to the heat exchangers located at the bottom of the setup. This arrangement provides stable thermal conditions throughout the loop, ensuring that the electrolyte and cell operate within the desired temperature range.

Two pressure sensors are installed—one on the anode side and one on the cathode side. These sensors continuously measure the internal pressure of each compartment, providing real-time data that can be used to verify system stability and to detect possible imbalances between the two sides. The recorded pressure values are expressed in bars (bar) and are crucial for identifying early signs of leaks, gas buildup, or flow obstructions within the loop.

Two anion exchange membrane water electrolyzer cells with an active area of 25 cm^2 were assembled, tested and operated at a controlled temperature of 60 °C and under atmospheric pressure. Both configurations consisted of a catalyst-coated membrane (CCM) sandwiched between a cathode gas diffusion layer (GDL) and a metallic anode, and were enclosed between two endplates, with a clamping force high enough that the high-frequency resistance (HFR) from EIS measurements no longer varied with further increases in clamping force. The EIS was performed in galvanostatic conditions.

Cell 1 employed a GDL made of Toray H60 containing 5% PTFE, followed by a 100 µm PTFE layer and an additional 25 µm PFA layer. The cathode is the CCM, which consisted of a PtRuC catalyst layer with a metal loading of 0.3 mg·cm^{-2} and an 80 µm PiperION membrane. The anode was made of SS316L stainless steel, comprising two 150 µm PTFE layers and one 25 µm PFA layer.

Cell 2 shared the same structural design for both the cathode and the anode, but the CCM differed slightly: it used a PtRuC catalyst with a higher loading (0.36 mg·cm^{-2}) and included 5% Nafion as an ionomer binder. The membrane was again an 80 µm PiperION layer.

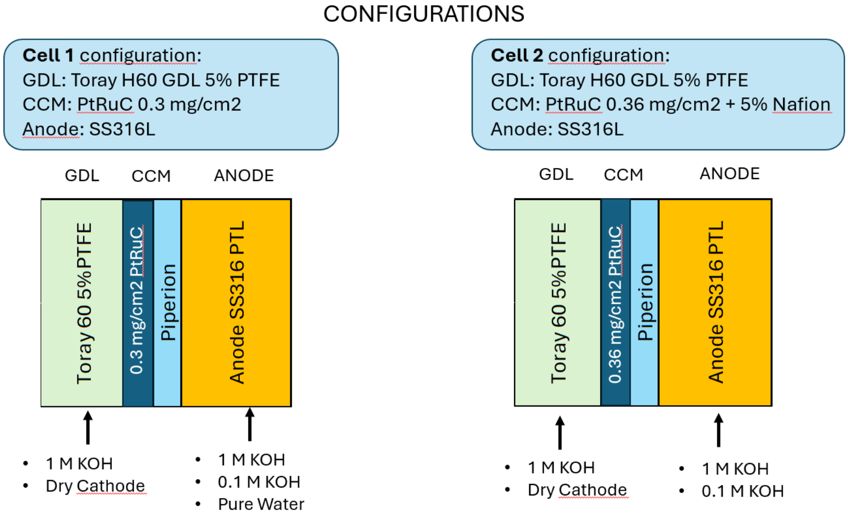

Figure 3.5: Cells configurations

During operation, both cells were tested under KOH-fed conditions, either supplying electrolyte to both anode and cathode sides, or exclusively to the anode while maintaining the cathode under dry conditions.

In both experimental cells, a reference electrode was employed at the anode and at the cathode to allow precise and independent measurement of each half-cell potential [Zhang and Bard, 2021]. The reference electrode provides a stable and reproducible potential, serving as a fixed baseline against which the working electrode potential can be accurately measured or controlled [Orazem and Tribollet, 2020]. In electrochemical systems, the absolute potential of an electrode cannot be directly determined, so a reference electrode with a constant potential is required to define the potential of the working electrode [Lasia, 2019].

Using a reference electrode at both sides of the system allows independent monitoring of anodic and cathodic potentials, which is crucial in systems where each electrode exhibits different reaction mechanisms or overpotential behaviors [Sathiya et al., 2023]. This configuration enables the separation of individual electrode contributions to the total cell voltage, improving the accuracy of kinetic analyses and electrochemical impedance spectroscopy fitting [Lasia, 2019]. Moreover, having reference electrodes in both half-cells permits the detection of degradation phenomena such as corrosion, passivation, or potential drift over time, ensuring that any voltage changes originate from electrochemical processes rather than instrumental instability or counter-electrode effects [Zhang and Bard, 2021].

3.2 Preparation of 1 M KOH Solution from Solid Pellets and 0.1 M KOH

To prepare 1 L of a 1 M potassium hydroxide (KOH) aqueous solution, the amount of solid KOH required can be calculated from its molar mass. Potassium hydroxide consists of one potassium atom (K), one oxygen atom (O), and one hydrogen atom (H). The molar mass is:

$$M_{\mathrm{KOH}} = M_{\mathrm{K}} + M_{\mathrm{O}} + M_{\mathrm{H}}$$

$$M_{\mathrm{KOH}} = 39.10 + 16.00 + 1.01 = 56.11\ \mathrm{g\,mol^{-1}}$$

For a solution of concentration $c = 1\ \mathrm{mol\,L^{-1}}$ and volume $V = 1$ L, the number of moles of solute needed is:

$$n = c \times V = 1\ \mathrm{mol\,L^{-1}} \times 1\ \mathrm{L} = 1\ \mathrm{mol}$$

The corresponding mass m of KOH is obtained from:

$$m = n \times M_{\mathrm{KOH}} = 1\ \mathrm{mol} \times 56.11\ \mathrm{g\,mol^{-1}} = 56.11\ \mathrm{g}$$

Therefore, to prepare 1 L of a 1 M KOH solution 56.11 g of KOH pellets to be dissolved in distilled water are necessary. Mixing the solution in a magnetic stirrer to ensure complete dissolution (Figure 3.6a).

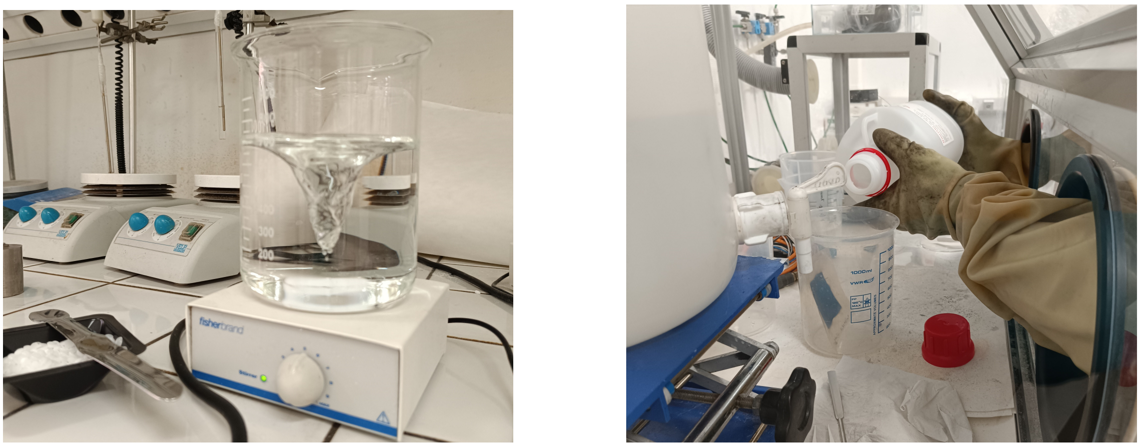

(a) 1 M KOH preparation in the magnetic stirrer

(b) 0.1 M KOH preparation in the nitrogen glove box

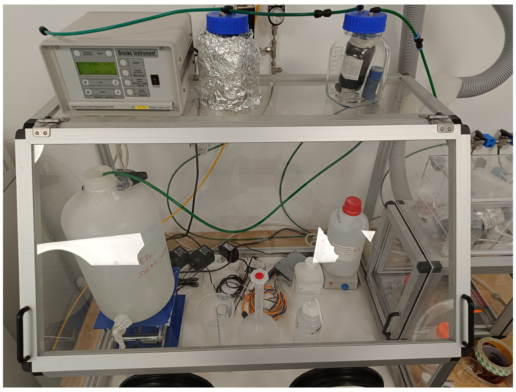

(c) Glove box with inert nitrogen atmosphere

Figure 3.6: KOH preparation

Since the dissolution of KOH in water is highly exothermic, the pellets were added slowly to a portion of water under stirring to avoid overheating or splashing.

To prepare 1 L of a 0.1 M KOH solution, 0.1 L of a 1 M KOH stock solution was diluted with deionized water to a final volume of 1 L. The preparation was performed inside the glove box with inert nitrogen atmosphere to prevent the reaction between KOH and atmospheric CO_2, which would otherwise lead to the formation of potassium carbonate (K_2CO_3) (Figure 3.6b). The presence of carbonate impurities can alter the electrolyte composition, reduce the effective hydroxide concentration, and affect both conductivity and electrochemical performance. Working under an inert N_2 atmosphere (Figure 3.6c) ensures the chemical stability and purity of the KOH solution, preserving its intended concentration and preventing unwanted side reactions.

Chapter 4

Results and Discussion

Figure 4.1 shows the performance of cell 1 as a function of the support electrolyte concentration. When the cathode was kept dry while feeding 1 M KOH only at the anode, the cell exhibited the lowest overall voltage at a given current density, indicating reduced ohmic and activation losses due to improved ionic conductivity.

When both electrodes were supplied with 1 M KOH, a slight increase in cell voltage was observed, especially in the high-current region, suggesting a moderate rise in resistance at the membrane–cathode interface. Reducing the supporting electrolyte concentration to 0.1 M KOH resulted in a further voltage increase, which can be attributed to lower electrolyte conductivity and reduced ionic transport efficiency through the membrane. Finally, when pure deionized water was supplied at the anode with a dry cathode, the cell performance decreased significantly, due to the minimal availability of mobile hydroxide ions and the consequent increase in overpotentials.
Focusing on the magnified inset, which represents the low-current-density region (0-0.04 A cm^{-2}), the activation overvoltages dominate. In this regime, the curves diverge significantly, reflecting differences in the intrinsic catalytic activity and electrode/electrolyte interface behavior under various hydration and ionic conditions. Pure-water curve shows delayed activation, requiring higher potential compared to both 1 M and 0.1 M KOH.

The polarization curve of cell 2, shown in Figure 4.2, exhibits a similar overall trend to that previously discussed for cell 1, confirming the same electrochemical behavior under varying electrolyte conditions. The cell fed with 1 M KOH at anode leaving dried the cathode displays the best performance starting from current densities of 0.3 A cm^{-2}, while the configuration run at the same concentration feeding both the cathode and the anode show progressively higher overvoltages for the same current density. The worst scenario is given by the reduced supporting electrolyte concentration 0.1 M KOH. For the

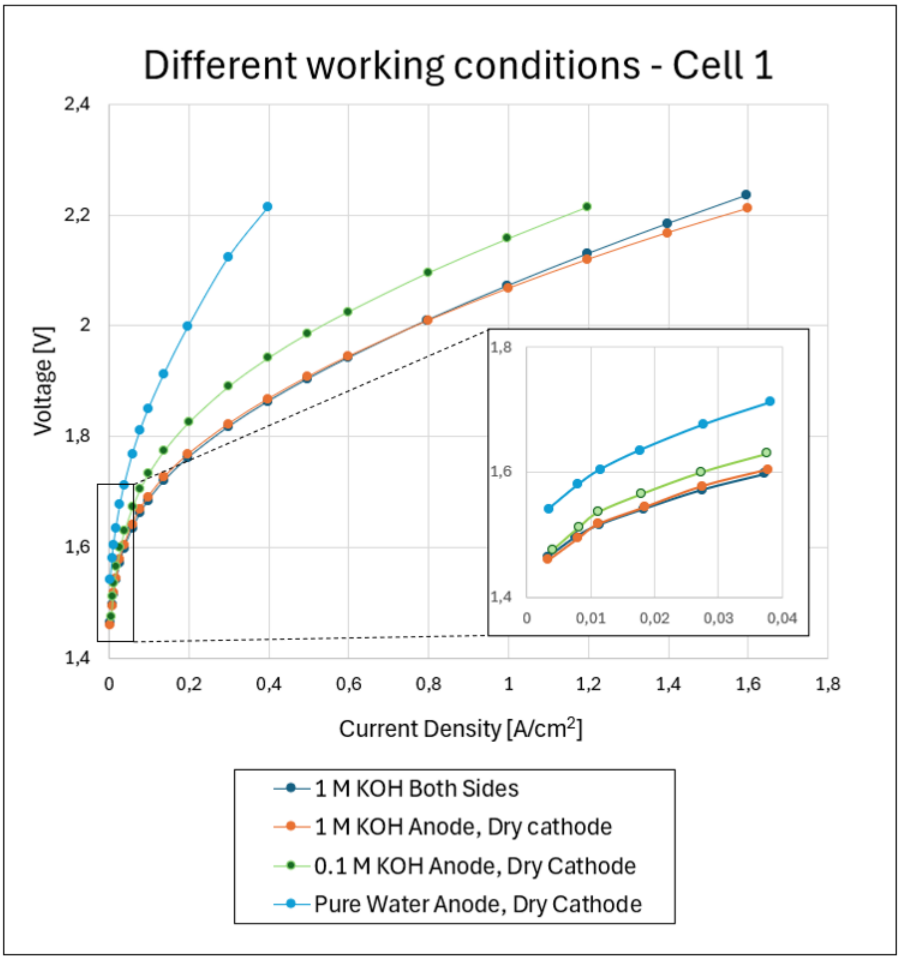

Figure 4.1: Polarisation curves, cell 1

same reasons already explained above—namely the combined effects of ionic conductivity and hydroxide availability—the slope of the curve increases as the electrolyte becomes less conductive.

In the zoomed-in view, focusing on the low-current-density region (0–0.1 A cm^{-2}), the activation domain is clearly visible. In this region, the best performance is provided by the both-feeding configuration, indicating that maintaining the cathode dry leads to a noticeable deterioration of the overall cell behavior during the activation regime. This effect can be attributed to insufficient wetting of the cathode catalyst layer, which limits the effective electrochemical surface area. Moreover, the lack of a continuous electrolyte film increases the local resistance and slows down the initial reaction kinetics, resulting in higher overpotentials at low current densities.

Overall, the cells exhibit superior performance in dry cathode configuration primarily due to electro-osmotic effects. Electro-osmosis refers to the directional transport of water

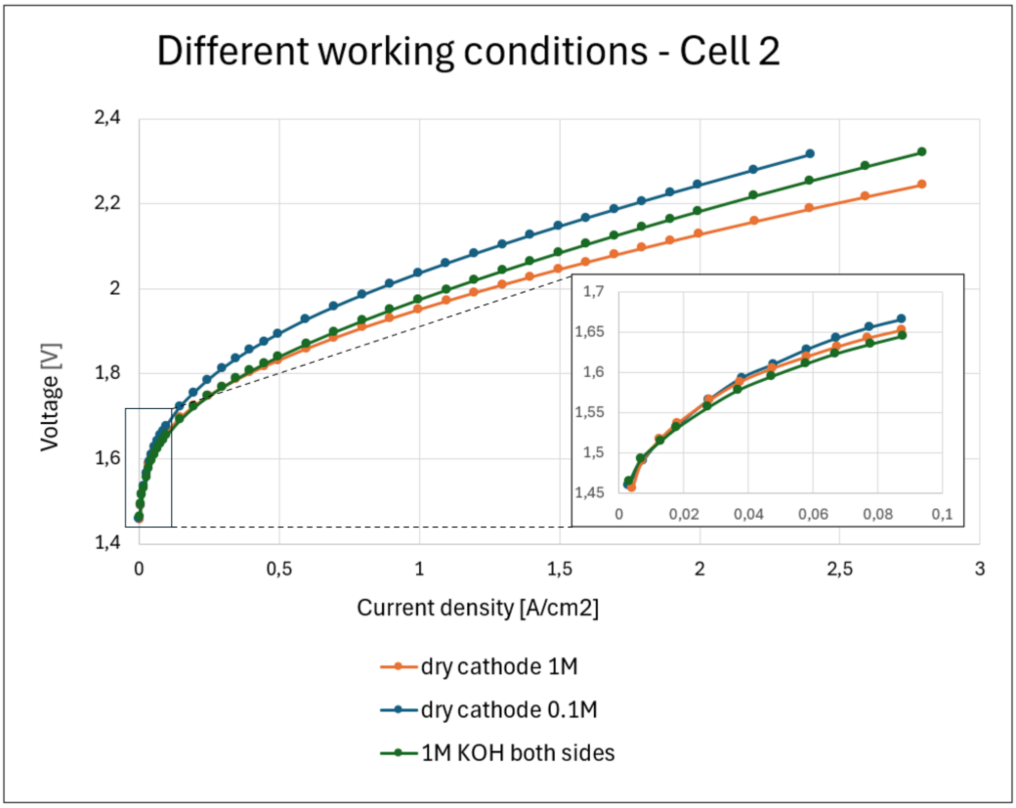

Figure 4.2: Polarisation curves, cell 2

molecules driven by the migration of charged species through an ion-conducting medium under an applied electric field. In alkaline or proton-conducting membranes, hydrated ions carry water as part of their solvation shell, producing a net water flux toward the electrode where the ions are moving. This phenomenon arises from electrostatic interactions between the mobile ions and the surrounding dipolar water molecules, resulting in a coupled mass–charge transport process [Yuan et al., 2021]. In this experiment, when operating in the both-feed mode, hydroxide ions (OH^-) migrate from the cathode toward the anode, dragging along water molecules through electro-osmotic transport. This water transfer leads to a dilution of the KOH concentration at the anode side. As a result, the supporting electrolyte becomes less concentrated, thereby exhibiting weaker ionic conductivity and overall electrochemical performance.

Conversely, in the dry cathode mode, only water molecules migrate from the anode to the cathode (H_2O osmosis), which in turn increases the KOH concentration at the anode. This enhanced concentration improves the electrolyte properties and consequently the overall cell performance.

This concept is shown in Figure 4.3 [Rosales].

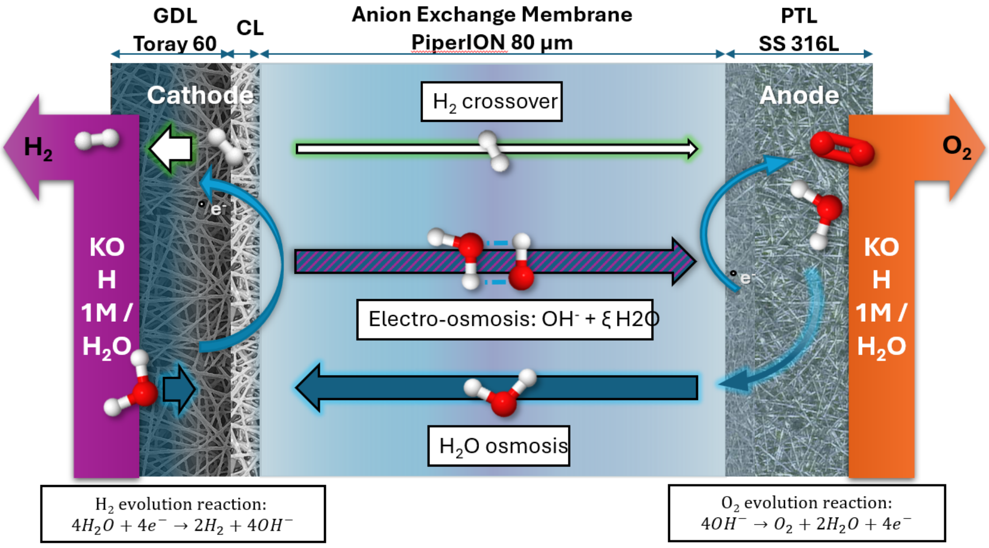

Figure 4.3: Water management: electro-osmosis and H_2O osmosis [Rosales]

Figure 4.4 compares the polarization behavior of cell 1 and cell 2 operated with a dry cathode and 1 M KOH as the anodic supporting electrolyte.
The voltage–current characteristics reveal a consistent performance enhancement in cell 2 across the entire current density range. At low current densities ($< 0.1\ \mathrm{A\,cm^{-2}}$), the inset magnifies this region, showing that cell 2 displays a slightly lower activation loss, which can be attributed to the presence of 5% Nafion within the CCM. This additive likely improves protonic pathways and enhances catalyst utilization. The reasons for the improvement are still being investigated.

As the current density increases, the voltage difference between the two cells becomes more pronounced, suggesting a cumulative reduction in ohmic and mass-transport losses in cell 2, as shown in 4.4. The optimized catalyst loading ($0.36\ \mathrm{mg\,cm^{-2}}$ vs. $0.30\ \mathrm{mg\,cm^{-2}}$ in cell 1) and the improved ionic connectivity of the membrane–electrode interface contribute to this behavior. Consequently, cell 2 achieves lower overall voltages at equivalent current densities, demonstrating a more efficient electrochemical performance under identical operating conditions.

The EIS results of Cell 1 are shown under two operating conditions: the first with 1 M KOH fed to both anode and cathode in Figure 4.5, and the second with a dry cathode and 0.1 M KOH supplied only to the anode side in Figure 4.6.

In both Nyquist plots, the real and imaginary components of the impedance are reported as Re(Z) and $-Im(Z)$ respectively, and each colored locus corresponds to a fixed total

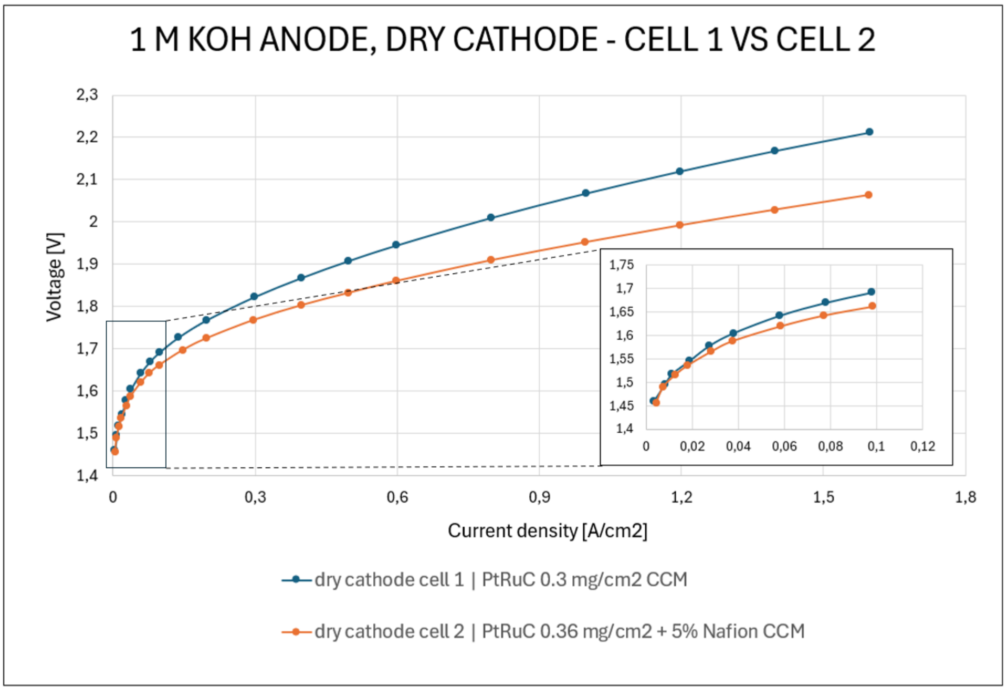

Figure 4.4: Comparison between cell 1 and cell 2 - 1 M KOH anode, dry cathode

current ranging from 1 to 25 A, 0.04–1 A cm^{-2} range in terms of current densities. All spectra exhibit depressed semicircles, a characteristic feature of non-ideal double-layer behavior that can be accurately modeled by a CPE instead of a pure capacitor. The diameter of the arcs decreases systematically with increasing current, indicating a progressive reduction of charge-transfer resistance as the overpotential increases.

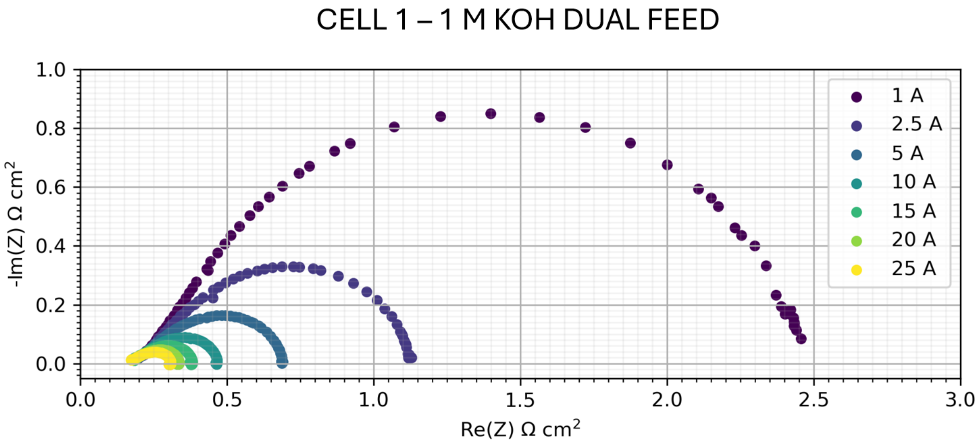

Figure 4.5: Electrochemical impedance spectroscopy cell 1 - 1 M KOH both feed

A comparison between the two operating conditions reveals that the configuration with 1 M KOH fed on both sides displays smaller semicircles and lower intercepts at every

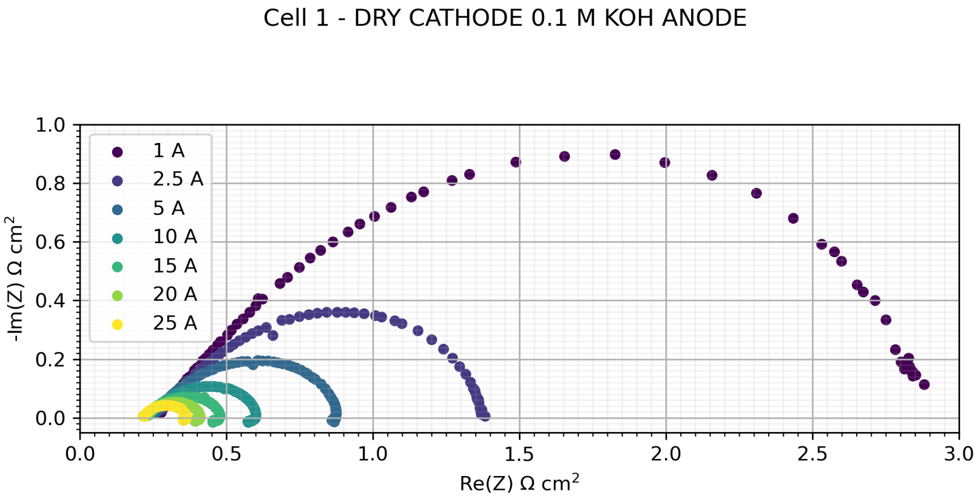

Figure 4.6: Electrochemical impedance spectroscopy cell 1 - 1 M KOH anode, dry cathode

current level, highlighting reduced ohmic and interfacial losses, as shown in figures 4.5 and 4.6. Specifically, the high-frequency intercept, corresponding to the uncompensated series resistance R_s, is approximately 0.15–0.20 $\Omega{\cdot}\text{cm}^2$ in the both-feed case, while it increases to about 0.20–0.25 $\Omega{\cdot}\text{cm}^2$ when only the anode is wetted with 0.1 M KOH. This difference confirms the higher ionic conductivity was improved by higher concentrated electrolyte. Likewise, the low-frequency intercepts, representing the sum of R_s and R_{ct}, are consistently smaller in the both-feed configuration, suggesting lower charge-transfer resistance. In contrast, diluted electrolyte penalizes the interfacial kinetics and hinder ionic transport through the porous layers, thereby increasing the overall resistance.

At low current densities (0.04–0.1 A cm^{-2}), the spectra obtained with the dry-cathode/0.1 M KOH configuration exhibit broader and more elongated arcs, peaking at higher $-Im(Z)$ values, which is indicative of greater interfacial resistance and stronger dispersion effects, as shown in 4.6. In the both-feed 1 M KOH case Figure 4.5, the semicircles are smaller and closer to the origin, reflecting faster electrode kinetics and a narrower distribution of relaxation times. As the current increases from 5 to 15 A (0.2–0.6 A cm^{-2}), both spectra contract toward the origin, although the difference between the two conditions remains approximately constant, suggesting that the dominant contribution to the total resistance arises from ohmic and activation processes rather than from mass-transport limitations. At the highest currents 20 and 25 A (0.8 and 1 A cm^{-2}), the arcs become very small and nearly collapse toward the origin, indicating that mass-transport resistances are minimal, particularly under the both-feed condition.

A quantitative comparison of figures 4.5 and 4.6 can be made by examining the equivalent points on the two spectra, like for example the curves at 10 A and 2.5 A (0.4 and 0.1 A cm^{-2}). At 0.4 A cm^{-2}, the high-frequency intercept R_s is approximately 0.18 Ω·cm^2 for the both-feed configuration and around 0.23 Ω·cm^2 for the dry-cathode/0.1 M case. This increase of about 0.05 Ω·cm^2 reflects the effect of reduced electrolyte conductivity. Similarly, at 0.1 A cm^{-2}, the total resistance estimated from the low-frequency intercept ($R_s + R_{ct}$) is approximately 1.15 Ω·cm^2 for the both-feed configuration and 1.40 Ω·cm^2 for the dry-cathode configuration. The resulting difference of roughly 0.25 Ω·cm^2 highlights the additional interfacial losses introduced by the lower hydroxide concentration.

The EIS of cell 2 operated in dual-feed mode with 1 M KOH on both anode and cathode is shown in Figure 4.7. Measurements were performed up to 50 A, corresponding to a current density of approximately 2 A cm^{-2}.

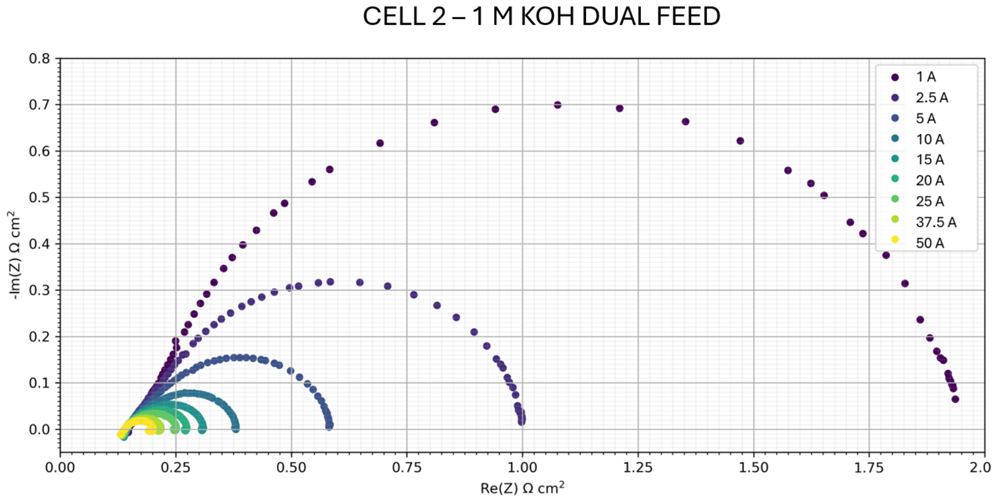

Figure 4.7: Electrochemical impedance spectroscopy cell 2 - 1 M KOH both feed

All Nyquist plots exhibit a single, depressed semicircle whose diameter progressively decreases with increasing current, indicating a marked reduction of charge-transfer resistance (R_{ct}) as the overpotential rises. The arcs remain compact and symmetric across the entire current range, confirming stable interfacial kinetics and negligible mass-transport limitations even at high current densities.

The high-frequency intercepts on the real axis, which correspond to the series resistance (R_s), lie between 0.12 and 0.15 Ω·cm^2, slightly lower than those measured for cell 1 under the same dual-feed 1 M KOH conditions, where R_s was approximately 0.15–0.20 Ω·cm^2. At low currents from 1 to 5 A (0.04–0.2 A cm^{-2}), the semicircles are still clearly visible, showing that activation polarization contributes to the total impedance; however, the consistent contraction of the arcs between 10 and 50 A (0.4 and 2 A cm^{-2}) demonstrates that the cell preserves efficient charge-transfer kinetics and stable electrode–electrolyte interfaces.

The Tafel plot shown in Figure 4.8 illustrates the Tafel behavior of cell 1 anode operated in both dual-feed and dry cathode configurations.

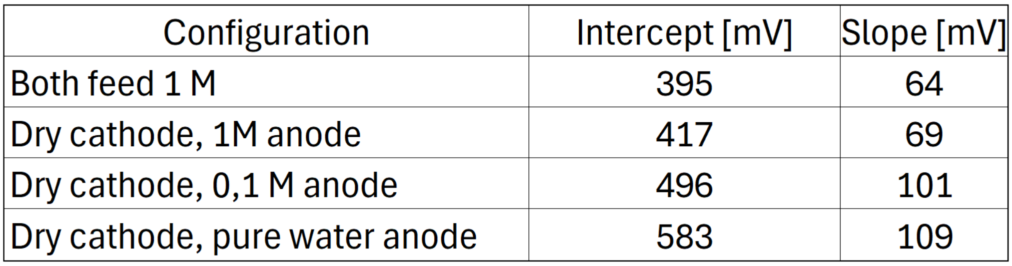

Configuration	Intercept [mV]	Slope [mV]
Both feed 1 M	395	64
Dry cathode, 1M anode	417	69
Dry cathode, 0,1 M anode	496	101
Dry cathode, pure water anode	583	109

Figure 4.8: Tafel intercept and slope for cell 1 anode

The results confirm that decreasing the KOH concentration leads to a reduction in electrochemical performance, as both the intercept and the Tafel slope are significantly higher in the 0.1 M and pure water cases compared to the 1 M case. This indicates increased overpotentials and slower reaction kinetics at lower electrolyte concentrations, consistent with the diminished ionic conductivity and catalytic activity expected under such conditions.

The Nyquist plot shown in Figure 4.10 compares the experimental impedance data with the curve simulated using the modified Randles equivalent circuit incorporating two constant-phase elements (CPEs) following the equivalent circuit in Figure 4.9.

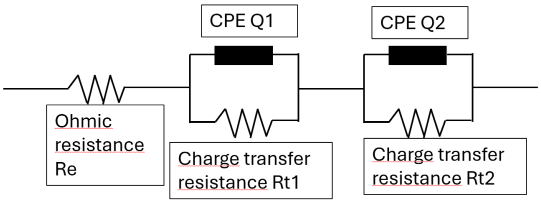

Figure 4.9: Equivalent electric circuit

The use of two CPEs is appropriate for modelling the full electrochemical cell, as it accounts for the non-ideal capacitive responses of both the anodic and cathodic interfaces.

The experimental data (black symbols) form a well-defined depressed semicircle, whose

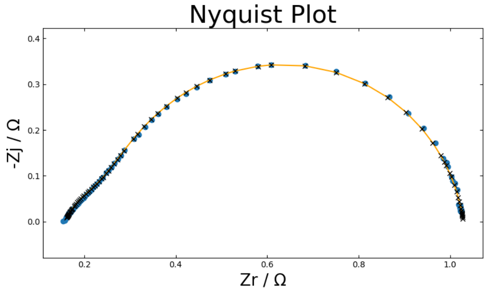

Figure 4.10: Parameter estimation for cell 2 - both feed 1 M

curvature and symmetry are accurately captured by the fitted model (orange line), confirming the adequacy of the equivalent circuit in describing the system behaviour.
The close overlap between the experimental points and the simulated curve demonstrates that the double-CPE configuration successfully reproduces both the magnitude and phase of the measured impedance across the entire frequency range.
The values of the area-specific resistance (ASR) are reported in Ω cm^2 in the Figure 4.11.

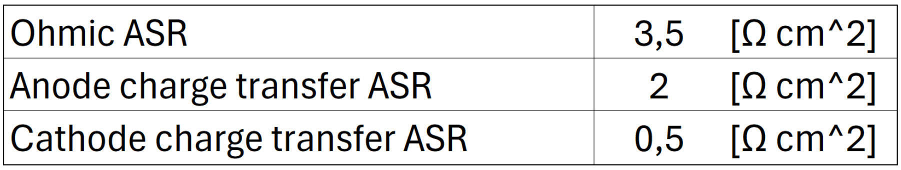

Ohmic ASR	3,5	[Ω cm^2]
Anode charge transfer ASR	2	[Ω cm^2]
Cathode charge transfer ASR	0,5	[Ω cm^2]

Figure 4.11: Resistances estimation

Chapter 5

Conclusions and perspectives

This work investigated the influence of the support electrolyte concentration on the electrochemical performance of AEMWE cells. Two experimental configurations were tested under identical operating conditions (60 °C, ambient pressure) but with different KOH concentrations and feeding modes, in order to elucidate the interplay between ionic conductivity, electrode kinetics, and electro-osmotic effects.

Polarisation and Tafel analyses revealed that the concentration of the KOH solution strongly affects both activation and ohmic overvoltages. In particular, cells operated with 1 M KOH exhibited significantly lower total overpotential compared to those with 0.1 M KOH, confirming that a higher ionic strength enhances charge transport both within the membrane and at the electrode–electrolyte interfaces.
For cell 1, the overall cell voltage at 1 A cm^{-2} decreased from approximately 2.15 V (0.1 M KOH) to 2.07 V (1 M KOH), while cell 2, characterized by an optimized interface and catalyst loading, achieved around 1.95 V under the same conditions. Correspondingly, the cell 1 Tafel slope increased from 64 mV to 101 mV when the concentration dropped from 1 M to 0.1 M, indicating slower electrode kinetics at lower ionic strengths.

Electrochemical impedance spectroscopy further supported these observations. The high-frequency intercepts, corresponding to the series resistance R_s in cell 1, decreased from roughly 0.25 $\Omega\cdot cm^2$ at 0.1 M to 0.15 $\Omega\cdot cm^2$ at 1 M, highlighting the direct correlation between electrolyte concentration and ohmic losses. The charge-transfer resistance R_{ct} followed a similar trend, decreasing when moving from diluted to concentrated KOH, demonstrating improved catalytic activity and enhanced interface conductivity. The fitting of impedance spectra through a modified Randles model with two CPE elements confirmed that each electrode interface contributes independently to the overall impedance, while the parallel resistive network represents the global ionic transport within the membrane–electrode assembly.

Additionally, the comparison between dry cathode and both-feeding modes revealed that, although dual feed initially provides enhanced hydration and slightly lower activation losses, prolonged operation leads to performance decay due to electro-osmotic drag of water molecules from the cathode to the anode, which progressively dilutes the anode supporting electrolyte. Conversely, in dry cathode mode, the osmotic flux proceeds in the opposite direction, maintaining a more stable electrolyte composition and therefore a more consistent performance over time.

Overall, the results clearly demonstrate that electrolyte concentration is a key design parameter for AEMWE systems. Increasing the KOH concentration improves the performance of the cell.

Future work should focus on balancing these advantages with material stability, with particular emphasis on the development of new materials capable of operating under low-electrolyte concentration conditions, in order to further optimize AEM performance.

Bibliography

K. W. Ahmed and M. Fowler. Performance evaluation and durability analysis of nifecoox catalysts for alkaline water electrolysis in anion exchange membrane electrolyzers. *Catalysts*, 14(5):322, 2024. doi: 10.3390/catal14050322. URL `https://doi.org/10.3390/catal14050322`.

R. Bernat, M. Kovačič, B. Boškin, P. Gorgojo, and N. Jovanovič. Review of aem electrolysis research from the perspective of materials, design, and performance. *Energies*, 17:5030, 2024. doi: 10.3390/en17205030. URL `https://www.mdpi.com/1996-1073/17/20/5030`.

L. Bertuccioli, A. Chan, D. Hart, F. Lehner, B. Madden, and E. Standen. Development of water electrolysis in the european union. Technical report, Fuel Cells and Hydrogen Joint Undertaking, 2014. URL `https://www.fch.europa.eu/sites/default/files/FCHJU%20Electrolysis%20Study%20Final_0.pdf`.

G. J. Brug, A. L. G. van den Eeden, M. Sluyters-Rehbach, and J. H. Sluyters. The analysis of electrode impedances complicated by the presence of a constant phase element. *Journal of Electroanalytical Chemistry and Interfacial Electrochemistry*, 176(1-2):275–295, 1984. doi: 10.1016/S0022-0728(84)80324-1. URL `https://doi.org/10.1016/S0022-0728(84)80324-1`.

M. Carmo, D. L. Fritz, J. Mergel, and D. Stolten. A comprehensive review on pem water electrolysis. *International Journal of Hydrogen Energy*, 38(12):4901–4934, 2013. doi: 10.1016/j.ijhydene.2013.01.151. URL `https://www.sciencedirect.com/science/article/pii/S0360319913000957`.

K. Chand, A. Kumar, and S. Patel. Recent developments of membranes and electrocatalysts for the hydrogen production by anion exchange membrane water electrolysers: A review. *Arabian Journal of Chemistry*, 15(9):103–757, 2022. doi: 10.1016/j.arabjc.2022.103757. URL `https://www.sciencedirect.com/science/article/pii/S1878535222007571`.

Byoung-Yong Chang. Conversion of a constant phase element to an equivalent capacitor. *Journal of Electrochemical Science and Technology*, 11(3):318–321, 2020. doi: 10.33961/jecst.2020.00815. URL `https://www.jecst.org/upload/pdf/jecst-2020-00815.pdf`.

R. Chen, Z. Liu, and X. Zhao. Impact of catalyst reconstruction on the durability of anion exchange membrane water electrolysis. *ACS Sustainable Chemistry & Engineering*, 10(48):15732–15742, 2022a. doi: 10.1021/acssuschemeng.2c04855. URL `https://pubs.acs.org/doi/10.1021/acssuschemeng.2c04855`.

Y. Chen, L. Zhang, J. Wang, H. Liu, and C. Zhao. Dynamic surface reconstruction and element dissolution in nifeco anodes for alkaline water electrolysis. *Journal of Power Sources*, 543:231–561, 2022b. doi: 10.1016/j.jpowsour.2022.231561. URL `https://doi.org/10.1016/j.jpowsour.2022.231561`.

H. Choi, D. Park, and Y. Lee. Enhanced performance and durability of pore-filling membranes for anion exchange membrane water electrolysis. *Membranes*, 14:269, 2024. doi: 10.3390/membranes14120269. URL `https://doi.org/10.3390/membranes14120269`.

B. Endrődi, E. Kecsenovity, A. Samu, and C. Janáky. High carbonate ion conductance of a robust piperion membrane allows industrial current density and conversion in a zero-gap carbon dioxide electrolyzer cell. *Energy & Environmental Science*, 13:4098–4105, 2020. doi: 10.1039/D0EE02589E. URL `https://doi.org/10.1039/D0EE02589E`.

European Commission. Communication: The european green deal. Communication from the Commission to the European Parliament, the European Council, the Council, the European Economic and Social Committee and the Committee of the Regions, 2019. URL `https://commission.europa.eu/publications/communication-european-green-deal_en`.

European Commission. Repowereu: Joint european action for more affordable, secure and sustainable energy. Communication from the Commission to the European Parliament, the European Council, the Council, the European Economic and Social Committee and the Committee of the Regions, 2022. URL `https://eur-lex.europa.eu/legal-content/EN/TXT/?uri=CELEX:52022DC0230`.

European Commission. European green deal and repowereu plan, 2023. URL `https://commission.europa.eu/strategy-and-policy/priorities-2019-2024/european-green-deal_en`.

European Commission / European Parliament. The “fit for 55” package: Delivering the eu’s 2030 climate target on the way to climate neutrality. European Union policy package, 2021. URL `https://www.europarl.europa.eu/RegData/etudes/BRIE/2022/733513/EPRS_BRI(2022)733513_EN.pdf`. Legislative proposals and briefings under the European Green Deal.

D.Y. Gavrailov and S.V. Boycheva. Study assessment of water electrolysis systems for green production of pure hydrogen and natural gas blending. *IOP Conference: Series Earth and Environmental Science*, 2023. URL `https://www.researchgate.net/publication/373888487_Study_assessment_of_water_electrolysis_systems_for_green_production_of_pure_hydrogen_and_natural_gas_blending`.

D. George and R. K. Singh. Recent advances in nickel-based anodes for anion exchange membrane water electrolyzers. *Journal of Materials Chemistry A*, 13(4):1458–1472, 2025. doi: 10.1039/d5ta05931c. URL `https://pubs.rsc.org/en/content/articlelanding/2025/ta/d5ta05931c`.

L. Guo, F. Wang, X. Chen, and J. Liu. Highly conductive and stable electrolytes for solid oxide electrolysis cells. *Materials Advances*, 2025. doi: 10.1039/D4MA00690A. URL `https://pubs.rsc.org/en/content/articlehtml/2025/ma/d4ma00690a`.

N. Hallemans, D. A. Howey, A. Battistel, N. F. Saniee, F. Scarpioni, B. Wouters, F. La Mantia, A. Hubin, W. D. Widanage, and J. Lataire. Electrochemical impedance spectroscopy beyond linearity and stationarity – a critical review. *Electrochimica Acta*, 460:142304, 2023. doi: 10.1016/j.electacta.2023.142304. URL `https://doi.org/10.1016/j.electacta.2023.142304`.

C. Hsu and F. Mansfeld. Technical note: Concerning the conversion of the constant phase element parameter y_0 into a capacitance. *Corrosion*, 57(9):747–748, 2001. doi: 10.5006/1.3280607. URL `https://content.ampp.org/corrosion/article/57/9/747/6559/Technical-Note-Concerning-the-Conversion-of-the`.

L. Hu, Y. Zhao, C. Xu, and Q. Zhang. High conductivity and alkaline stability of anion exchange membranes containing multiple flexible side-chain piperidinium ions. *Materials Chemistry Frontiers*, 5:7144–7154, 2021. doi: 10.1039/D1QM00826A. URL `https://doi.org/10.1039/D1QM00826A`.

Hydrogeninsight. Global investment in clean hydrogen production expected to grow by 70% in 2025: Iea, 2025. URL `https://www.fuelcellchina.com/Industry_information_details/6353.html`.

Intergovernmental Panel on Climate Change (IPCC). Climate change 2023: Synthesis report. contribution of working groups i, ii and iii to the sixth assessment report of the ipcc, 2023. URL `https://www.ipcc.ch/report/ar6/syr/`.

International Energy Agency. World energy outlook 2024, 2024. URL `https://www.iea.org/reports/world-energy-outlook-2024`.

Hiroshi Ito, Naoki Miyazaki, Shota Sugiyama, Masayoshi Ishida, Yuka Nakamura, Shinya Iwasaki, Yasuo Hasegawa, and Akihiro Nakano. Investigations on electrode configurations for anion exchange membrane electrolysis. *Journal of Applied Electrochemistry*, 48(3):305–316, 2018. doi: 10.1007/s10800-018-1159-5. URL `https://doi.org/10.1007/s10800-018-1159-5`.

S. S. Kumar and H. Vurimindi. Hydrogen production by pem water electrolysis – a review. *Materials Science for Energy Technologies*, 2(2):442–454, 2019. doi: 10.1016/j.mset.2019.03.002. URL `https://doi.org/10.1016/j.mset.2019.03.002`.

A. Lasia. The importance of reference electrodes in electrochemical impedance spectroscopy studies. *Electrochimica Acta*, 320(8):134589, 2019. doi: 10.1016/j.electacta.2019.134589. URL `https://doi.org/10.1016/j.electacta.2019.134589`.

A. C. Lazanas et al. Electrochemical impedance spectroscopy: A tutorial. *ACS Measurement Science Au*, 3(4):429–456, 2023. doi: 10.1021/acsmeasuresciau.2c00070. URL `https://pubs.acs.org/doi/10.1021/acsmeasuresciau.2c00070`.

C. Li, Z. Gao, and Y. Yang. Durability issues of protonic ceramic electrolysis cells: Materials and degradation mechanisms. *Energy Science & Engineering*, 10(9):2490–2506, 2022. doi: 10.1002/ese3.1010. URL `https://scijournals.onlinelibrary.wiley.com/doi/full/10.1002/ese3.1010`.

F. Lopez, S. Tanaka, and R. Singh. Long-term stability for anion exchange membrane water electrolysis: Recent development and future perspectives. *Future Batteries*, 2:100045, 2025. doi: 10.1016/j.fbat.2025.100045. URL `https://www.sciencedirect.com/science/article/pii/S2950264025000036`.

J. Luo. *Feasibility of Flexible CO2 Conversion Technologies Powered by Renewable Electricity. A conceptual case study of microbial electrosynthesis*. PhD thesis, Delft University of Technology, 2024.

J. R. Macdonald. Impedance spectroscopy. *Annals of Biomedical Engineering*, 20:289–305, 1992. doi: 10.1007/BF02368532. URL `https://link.springer.com/article/10.1007/BF02368532`.

M. Mamlouk and K. Scott. Alkaline stability of quaternary ammonium cations for alkaline fuel cell membranes and ionic liquids. *Journal of Power Sources*, 288:264–275, 2015. doi: 10.1016/j.jpowsour.2015.04.093. URL `https://doi.org/10.1016/j.jpowsour.2015.04.093`.

P. Millet, S. A. Grigoriev, and V. N. Fateev. Electrochemical technologies for hydrogen production from water electrolysis. *Electrochimica Acta*, 295:873–891, 2019. doi: 10.1016/j.electacta.2018.10.208. URL `https://www.sciencedirect.com/science/article/pii/S0013468618324170`.

M. Montalto, F. Rossi, A. De Luca, and P. Bianchi. Spinel-type high-entropy oxides for enhanced oxygen evolution reaction activity in anion exchange membrane water electrolyzers. *Journal of Electrochemical Energy Conversion and Storage*, 22(2):85–98, 2025. doi: 10.1016/j.jeecs.2024.03.015. URL `https://www.journals.elsevier.com/journal-of-electrochemical-energy-conversion-and-storage`.

H. Nguyen, Y. Park, and J. Lee. Low-cost and high-performance anion-exchange membrane water electrolysis stack using non-noble metal-based materials. *ACS Applied Energy Materials*, 6(2):1435–1445, 2023. doi: 10.1021/acsaem.3c01215. URL `https://pubs.acs.org/doi/abs/10.1021/acsaem.3c01215`.

M. E. Orazem and B. Tribollet. Advances in reference electrode design for accurate impedance measurements. *Electrochimica Acta*, 354(5):136729, 2020. doi: 10.1016/j.electacta.2020.136729. URL `https://doi.org/10.1016/j.electacta.2020.136729`.

Mark E. Orazem and Bernard Tribollet. *Electrochemical Impedance Spectroscopy*. Wiley, Hoboken, NJ, 2 edition, 2017. ISBN 9781119523703. URL `https://www.wiley.com/en-us/Electrochemical%2BImpedance%2BSpectroscopy%2C%2B2nd%2BEdition-p-9781119363682`.

J. Park, Y. Cho, and Y. Sung. Unified anodes with different nickel–iron-based phases for durable aem electrolyzers achieving high performance of 8000 ma cm^{-2} at 2.05 v. *Journal of Materials Chemistry A*, 13(4):1550–1562, 2025. doi: 10.1039/D5TA05065K. URL `https://doi.org/10.1039/D5TA05065K`.

I. V. Pushkarev, A. S. Pushkareva, S. A. Grigoriev, P. Modisha, and D. G. Bessarabov. Electrochemical impedance spectroscopy study of an aem water electrolyzer based on sustainion® membrane. *International Journal of Hydrogen Energy*, 48:12851–12862, 2023. doi: 10.1016/j.ijhydene.2023.01.204. URL `https://doi.org/10.1016/j.ijhydene.2023.01.204`.

W. Qi, L. Zhang, Y. Wu, and J. Chen. Stabilizing amorphous nife-based catalysts via borate bridging for water oxidation under industrial conditions. *Energy Advances*, 1 (5):500–512, 2025. doi: 10.1039/d5ea00111k. URL `https://pubs.rsc.org/en/content/articlehtml/2025/ea/d5ea00111k`.

J. E. B. Randles. Kinetics of rapid electrode reactions. *Discussions of the Faraday Society*, 1:11–19, 1947. doi: 10.1039/DF9470100011. URL `https://pubs.rsc.org/en/content/articlelanding/1947/df/df9470100011`.

M. Ranz, B. Grabner, B. Schweighofer, H. Wegleiter, and A. Trattner. Dynamics of anion exchange membrane electrolysis: Unravelling loss mechanisms with eis, reference electrodes and drt. *Journal of Power Sources*, 605: 234455, 2024. URL `https://tugraz.elsevierpure.com/en/publications/dynamics-of-anion-exchange-membrane-electrolysis-unravelling-loss`.

Transparency Market Research. Hydrogen electrolyzers market size, share forecast 2035, 2025. URL `https://www.transparencymarketresearch.com/hydrogen-electrolyzer-market.html`.

José Carlos Martinez Rosales. Water management: electro-osmosis and h_2o osmosis. Personal communication, September 2025.

N. N. Rosman, S. H. Lee, J. Kim, and T. Park. Nanostructured transition metal-based electrocatalysts: A promising pathway in anion exchange membrane water electrolysis. *Journal of Advanced Catalysis*, 10(1):1–14, 2025. doi: 10.1016/j.jacat.2025.01.001. URL `https://www.journals.elsevier.com/journal-of-advanced-catalysis`.

J. Salerno, J. Zhang, and E. Fisher. Anion exchange membranes derived from nafion precursor for the alkaline fuel cell: effect of cation type on properties. *Electrochimica Acta*, 114:589–596, 2013. doi: 10.1016/j.electacta.2013.09.122. URL `https://doi.org/10.1016/j.electacta.2013.09.122`.

K. Sathiya, H. Yang, and D. Lee. Advanced reference electrode architectures for accurate electrochemical measurements in energy systems. *Journal of The Electrochemical Society*, 170(7):070513, 2023. doi: 10.1149/1945-7111/acdc38. URL `https://doi.org/10.1149/1945-7111/acdc38`.

L. C. Seitz and A. T. Marshall. Anion exchange membrane water electrolysis: Opportunities and challenges. *Nature Energy*, 7(6):489–501, 2022. doi: 10.1038/s41560-022-01054-2. URL `https://www.nature.com/articles/s41560-022-01054-2`.

N. Sezer. A comprehensive review of the state-of-the-art of proton exchange membrane water electrolysis. *Materials Science for Energy Technologies*, 3(1):100–115, 2025. doi: 10.1016/j.mset.2025.01.005. URL `https://doi.org/10.1016/j.mset.2025.01.005`.

J. Smith and H. Lee. Ni_4mo alloys as highly active her catalysts for anion exchange membrane water electrolysis. *Electrochimica Acta*, 450:210–225, 2025. doi: 10.1016/j.electacta.2025.215678. URL `https://doi.org/10.1016/j.electacta.2025.215678`.

J. Smith, D. Kim, and T. Li. Efficient and durable anion exchange membrane water electrolysis for a commercially available electrolyzer stack using alkaline electrolyte. *ACS Energy Letters*, 7(12):4114–4122, 2022a. doi: 10.1021/acsenergylett.2c01049. URL `https://pubs.acs.org/doi/10.1021/acsenergylett.2c01049`.

J. Smith, H. Lee, and K. Tan. Improved oxygen evolution reaction kinetics with titanium incorporated nickel ferrite for efficient anion exchange membrane electrolysis. *ACS Catalysis*, 14(8):5632–5643, 2024. doi: 10.1021/acscatal.3c05761. URL `https://pubs.acs.org/doi/10.1021/acscatal.3c05761`.

T. Smith, J. Salerno, and C. Lewis. Quaternary ammonium-bearing perfluorinated polymers for anion exchange membrane applications. *Membranes*, 12:306, 2022b. doi: 10.3390/membranes12120306. URL `https://doi.org/10.3390/membranes12120306`.

Y. Tanaka and S. Kimura. Ni/ceo$_x$ interfaces for enhanced hydrogen evolution in aem water electrolysis. *Journal of Materials Chemistry A*, 13:345–360, 2025. doi: 10.1039/d4ta09876k. URL `https://doi.org/10.1039/d4ta09876k`.

UNFCCC. The glasgow climate pact (decision -/cp.26). Decision adopted by the Conference of the Parties to the UNFCCC at its 26th session, Glasgow, 2021. URL `https://unfccc.int/sites/default/files/resource/cop26_auv_2f_cover_decision.pdf`.

United Nations. Sustainable development goal 7: Ensure access to affordable, reliable, sustainable and modern energy for all. United Nations Sustainable Development Goals Knowledge Platform, 2015. URL `https://sdgs.un.org/goals/goal7`.

United Nations Framework Convention on Climate Change (UNFCCC). Paris agreement. Treaty text under the UNFCCC, 2015. URL `https://unfccc.int/sites/default/files/english_paris_agreement.pdf`.

I. Vincent, E.-C. Lee, and H.-M. Kim. Comprehensive impedance investigation of low-cost anion exchange membrane electrolysis for large-scale hydrogen production. *Scientific Reports*, 11(293), 2021. URL `https://www.nature.com/articles/s41598-020-80683-6`.

T. Volk, T. Lister, and Y. Yan. Role of the ionomer in supporting electrolyte-fed anion exchange membrane water electrolyzers. *Journal of the Electrochemical Society*, 172: 042518, 2025. doi: 10.1149/1945-7111/ad2e12. URL `https://doi.org/10.1149/1945-7111/ad2e12`.

C. Wang, D. Petrova, and M. Huang. Anion exchange membrane water electrolysis: The future of green hydrogen. *The Journal of Physical Chemistry C*, 127(14):6932–6945, 2023. doi: 10.1021/acs.jpcc.3c00319. URL `https://pubs.acs.org/doi/abs/10.1021/acs.jpcc.3c00319`.

C. R. Wang et al. Proton exchange membrane (pem) water electrolysis: Cell-level considerations for gigawatt-scale deployment. *Chemical Reviews*, 125(10):1234–1256, 2025. doi: 10.1021/acs.chemrev.3c00904. URL `https://doi.org/10.1021/acs.chemrev.3c00904`.

J. Wang, H. Li, Y. Zhou, and Q. Chen. Nife-based electrocatalysts for anion exchange membrane water electrolysis: activity and scalability. *Journal of Power Sources*, 620: 233–456, 2024. doi: 10.1016/j.jpowsour.2024.233456. URL `https://doi.org/10.1016/j.jpowsour.2024.233456`.

S. A. Watzele, K. J. J. Mayrhofer, and S. Cherevko. Impedance response analysis of anion exchange membrane electrolyzers: Modelling and spectral decomposition. *Chemistry Methods & Technologies*, 4:e202300035, 2024. doi: 10.1002/cmtd.202300035. URL `https://doi.org/10.1002/cmtd.202300035`.

H. Yassin, B. Kim, and C. Li. Loss analysis and optimization of piperion-based aem water electrolyzers. *ACS Applied Energy Materials*, 8:2251–2264, 2025. doi: 10.1021/acsaem.5c00045. URL `https://doi.org/10.1021/acsaem.5c00045`.

W. W. Yuan, K. Ou, S. Jung, and Y. B. Kim. Analyzing and modeling of water transport phenomena in fuel cells. *Applied Sciences*, 11(13):5964, 2021. doi: 10.3390/app11135964. URL `https://doi.org/10.3390/app11135964`.

K. Zeng and D. Zhang. Recent progress in alkaline water electrolysis for hydrogen production and applications. *Progress in Energy and Combustion Science*, 36(3):307–326, 2010. doi: 10.1016/j.pecs.2009.11.002. URL `https://www.sciencedirect.com/science/article/pii/S0360128509000613`.

Jin Zhang, Alexander F. Chadwick, and Peter W. Voorhees. Quantitative phase field model for electrochemical systems. *Journal of The Electrochemical Society*, 170(12): 120503, 2023. doi: 10.1149/1945-7111/acb1e8. URL `https://doi.org/10.1149/1945-7111/acb1e8`.

X. Zhang, Q. Liu, and J. Luo. Advancements, strategies, and prospects of solid oxide electrolysis cells (soecs) for hydrogen production. *International Journal of Hydrogen Energy*, 2024. URL `https://www.sciencedirect.com/science/article/abs/pii/S2095495624002237`.

Y. Zhang and A. J. Bard. Reference electrodes and their role in modern electrochemical measurements. *Journal of The Electrochemical Society*, 168(1):016510, 2021. doi: 10.1149/1945-7111/abd123. URL `https://iopscience.iop.org/article/10.1149/1945-7111/abd123`.

K. Zhao, Q. Wang, and et al. High-performance pure water-fed anion exchange membrane water electrolysis with patterned membrane via mechanical stress and hydration-mediated patterning technique. *Advanced Science*, 11(7):2400221, 2024. doi: 10.1002/advs.202400221. URL `https://onlinelibrary.wiley.com/doi/abs/10.1002/advs.202400221`.

Z. Zheng, B. Xue, J. Yao, Q. He, Z. Wang, and J. Yan. Ultramicroporous crosslinked polyxanthene–poly(biphenyl piperidinium)-based anion exchange membranes for water electrolyzers operating under highly alkaline conditions. *Materials Horizons*, 11: 6117–6125, 2024. doi: 10.1039/D4MH00836G. URL `https://doi.org/10.1039/D4MH00836G`.

Y. Zhou, H. Zhang, and H. Xu. Solid oxide electrolyzers process integration: A comprehensive review. *Processes*, 13(8):2656, 2025. doi: 10.3390/pr13082656. URL `https://www.mdpi.com/2227-9717/13/8/2656`.